

## Chapter 3

# A survey of CN, HCN, CO and HCO<sup>+</sup> emission from TTs and HAe disks

### Abstract

Models indicate that molecular line emission from CN, HCN and HNC should serve as good tracers of the temperature, UV and X-ray radiation fields in the surface layers of circumstellar disks. This is consistent with previous OVRO observations of T Tauri (LkCa 15 and GM Aur) and Herbig Ae disks (HD 163296 and MWC 480), which indicate that CN/HCN and HCO<sup>+</sup>/CO ratios increase with increasing UV field, where the UV field can be enhanced either via dust settling or due to a higher luminosity of the central star. In this work, we expand the previous study, choosing disks which have been previously mapped in CO and demonstrate Keplerian rotation, along with large disk masses and sizes, so that CN and HCN should be confined to the disks and observable. We have also chosen systems with a range of X-ray and optical luminosities and dust properties, as described by  $L_{FIR}/L_{bol}$  and stellar  $A_V$ , in order to examine whether the properties of the disk (dust settling) or the central star (radiation field) exert a stronger influence on the chemistry.

### 3.1 Introduction: Tracing temperature and radiation fields in circumstellar disks

A thorough understanding of the physical and chemical structure of disks around older T Tauri and Herbig Ae stars is important for constraining models of dust processing, settling, and agglomeration. It is also necessary for estimating the dispersal timescales for nebular gas and dust, the critical building blocks from which planets are assembled. Indeed, the amount of gas (and dust) available within an accretion disk and the timescale over which it is dissipated play major roles in determining what kind of planetary system, if any, can be formed. Furthermore, an understanding of how various volatile species (H<sub>2</sub>O, CO, CH<sub>4</sub>, NH<sub>3</sub>, N<sub>2</sub>, etc.) are distributed in the outer regions of

circumstellar disks is particularly important to examining the connection between interstellar and nebular processes in the formation of icy planetesimals such as comets and Kuiper Belt Objects.

The question of planet formation is intimately related to the formation and evolution of disks around protostars. Molecular line emission can be used to probe this special stage in the development of planetary systems. Until recently, most of the imaging of classical T Tauri and Herbig Ae stars outlined above was carried out in various isotopomers of CO for reasons of sensitivity. Through single dish surveys of several T Tauri stars, namely, DM Tau, GG Tau (Dutrey et al., 1997), TW Hya (Kastner et al., 1997), and LkCa 15 (van Zadelhoff et al., 2001), a number of species (HCN, CN, HNC, H<sub>2</sub>CO, HCO<sup>+</sup>, CS, ...) have been detected in several transitions, with emission intensities similar to that of <sup>13</sup>CO or C<sup>18</sup>O. High-resolution molecular line surveys of 4 disks (LkCa 15, MWC 480, GM Aur and HD 163296) with the OVRO interferometer have met with similar success (Qi, 2001; Qi et al., 2003). These important data suggest that, at least in appropriate disks, chemical studies regarding the nature and variation of the disk composition with radius can now be profitably pursued. They further reveal that both ion-molecule chemistry and photon-dominated chemistry must contribute to the observed abundances at large disk radii, since the ratios of species such as CN/HCN and HNC/HCN are too high to be accounted for by quiescent chemical models alone (Spaans, 1996, Dutrey et al., 1997, Kastner et al., 1997).

As van Zadelhoff (2002) shows, the high optical depth of many millimeter-wave transitions and the temperature gradients set up by the interaction of the disk with radiation from the central stars ensures that it is the upper regions of disk that are traced. At disk surfaces molecules can be dissociated by UV radiation, or ionized by UV photons, X-rays and cosmic rays. Recent surveys conducted with the Roentgen satellite (ROSAT) of T Tauri (Feigelson & Montmerle, 1999, Casanova et al., 1995, Neuhaeuser et al., 1995) and Herbig Ae/Be (Zinnecker & Preibisch, 1994) stars indicate that most are X-ray sources. The X-ray luminosity of T Tauri stars lies in the range 10<sup>29</sup>-10<sup>30</sup> erg s<sup>-1</sup> (Glassgold et al., 1997), which can drive ionization rates of  $\sim 5 \times 10^{-14}$  s<sup>-1</sup> at 1 AU. The standard ionization rate by cosmic rays is  $1.3 \times 10^{-17}$  s<sup>-1</sup>. Additionally, the protoplanetary disk is irradiated by UV photons from both the interstellar field and the central star. The UV flux from the central star and nearby stars may drive the total UV flux impinging on the disk to values as high as  $G_0 = 10^4 - 10^6$  Habing, (Herbig & Goodrich, 1986; Johnstone & Penston, 1986; Imhoff & Appenzeller, 1987; Montmerle, 1992), where 1 Habing =  $1.6 \times 10^{-3}$  ergs cm<sup>-2</sup> s<sup>-1</sup> is the estimated average flux in the local interstellar medium (Tielens & Hollenbach, 1985). Chemistry in the outermost near-surface regions of disks therefore shows similarities to both ion-molecule chemistry (Millar et al., 1991) and that in photon-dominated regions, or PDRs (Fuente et al., 1993; Jansen et al., 1995; Sternberg & Dalgarno, 1995).

Molecular line emission from CN, HCN and HNC should serve as good tracers of the disk environment in these surface regions. Fuente et al. (1993) show that although the abundance of most

Table 3.1. Effects of luminosity and dust settling on the CN/HCN ratio in disks

Source	Luminosity ( $L_{\odot}$ )	CN/ $^{13}\text{CO}$	$\text{HCO}^+/\text{}^{13}\text{CO}$	CN/HCN	H/h <sup>a</sup>
LkCa 15	0.72	$\sim 0.01$	$\sim 0.001$	$\sim 10$	1.0
GM Aur	0.8	$\sim 0.003^{\text{b}}$	$\ll 0.00025$	$\ll 1$	4.0
MWC 480	32.4	$\sim 0.007$	$\sim 0.001$	$\sim 4$	1.7
HD 163296	30.2	$\sim 0.01$	$\sim 0.0005$	$\gg 20$	2.0

<sup>a</sup>The ratio of the height of the disk photosphere and the vertical gas scale height from SED fits

<sup>b</sup>HCN/ $^{13}\text{CO}$  is used instead of CN/ $^{13}\text{CO}$

molecular species decreases with increasing UV radiation, some species increase at moderate UV fields (CH, CH<sup>+</sup>, CH<sub>2</sub>, CH<sub>2</sub><sup>+</sup>, CH<sub>3</sub><sup>+</sup>, C<sub>2</sub>, C<sub>2</sub>H and CN). Because of this behavior, CN and C<sub>2</sub>H are very sensitive to the presence of UV radiation and thus the luminosity of the central or nearby star(s). At high  $A_V$ , CN and HCN both can be formed from the dissociative recombination of the HCNH<sup>+</sup> ion. However, HCN can also be ionized by the fast reaction  $\text{HCN} + \text{H}^+ \rightarrow \text{HCN}^+ + \text{H}$ , and results in a decrease in the HCN abundance and an increase the CN/HCN ratio in these regions. This trend has been observed in PDRs; the CN/HCN ratio increases by a factor 15 (Fuente et al., 1993) from  $A_V=10$  mag (CN/HCN  $\sim 1$ ) to  $A_V=6$  mag (CN/HCN  $\sim 15$ ). The CN/HCN ratio has therefore been suggested as a tracer of enhanced UV fields. Since UV radiation is attenuated mainly by grains, UV photons will penetrate more deeply into the disk as grain sedimentation and growth proceed, and photochemistry will become more important. Additionally, models (Fuente et al., 1993) predict that the HNC/HCN ratio decreases by a factor of 5 from  $A_V=10 \rightarrow 6$  mag for a constant kinetic temperature of 30 K, and decreases by the same factor if the visual extinction is held constant but the kinetic temperature increases from 15 to 50 K. HNC/HCN will thus decrease with higher temperatures and stronger UV fields.

Initial OVRO observations of four disks indicate similar trends in the ratios of CN, HCN, and HCO<sup>+</sup> abundances (Qi, 2001; Table 3.1). The more luminous Herbig Ae stars MWC 480 and HD 163296 possess high CN/HCN and HCO<sup>+</sup>/CO ratios, likely due to increased photodissociation due to the higher UV flux of these stars. Among the two T Tauri stars, LkCa 15 and GM Aur, which have similar luminosity and spectral type, LkCa 15 has higher CN/HCN and HCO<sup>+</sup> ratios by factors of 10. This may be due to dust settling occurring in the LkCa 15 disk, indicated by a decrease in the ratio of the height of the dust photosphere to the gas pressure scale height (H/h). This ratio is calculated from fits to the SED for these disks (Chiang et al., 2001; discussed more below).

In this study, we expand the previous sample to include the sources in Table 3.2, chosen from previous CO surveys (Koerner & Sargent, 1995; Dutrey et al., 1996; Mannings & Sargent, 1997; Man-

Table 3.2. Source parameters

Source	Sp.Typ.	Age (Myr)	$A_V$	d (pc)	$M_D$ ( $M_\odot$ )	$M_G$ ( $M_\odot$ )	$R_{out}$ (AU)	$L_*$ ( $L_\odot$ )	$\log(L_X)$ (erg/s)	$L_{FIR}/L_{bol}$	Ref
AA Tau	M0Ve	0.45	0.84	140	0.018	...	150	1.5	29.53	0.15	6,8
AB Aur	B9/A0	3–5	0.65	160	0.01	1.3(-3)	450	53.6	29.52	<0.19	1,7,8
CQ Tau	A8Ve	10	0.96	100	0.015	2.62(-5)	<85	8.0	no obs.	0.50	2,9
DL Tau	K7	2	1.28	140	0.087	1.3(-6)	250	0.68	<30.04	0.33	3,6,8
DM Tau	M0.5	5	0.0	140	0.034	4(-3)	800	0.25	<29.66	0.16	4,5,6
Haro 6-5B	...	8.0	>0.02	140	0.021	0.45(-3)	150	...	no obs.	<0.02	5,8
MWC 758	A3e	6	0.22	200	0.005	3.97(-5)	185	20.6	no obs.	0.75	2,9
RY Tau	F8V:e	0.21	0.55	133	0.039	9.6(-6)	107	16.7	29.71	0.25	3,6,8

Note. — References: 1-Mannings & Sargent (1997), 2-Mannings & Sargent (2000), 3-Koerner & Sargent (1995), 4-Duvert et al. (2000), 5-Dutrey et al. (1996), 6-Damiani et al. (1995), 7-Zinnecker & Preibisch (1994), 8-Kenyon & Hartmann (1995), 9-Chiang et al. (2001).

nings & Sargent, 2000; Duvert et al., 2000), thanks to strong CO emission (0.4–3.2 Jy) whose emission patterns are consistent with models for isolated disks in Keplerian rotation. The sources selected are the largest ( $R_{out}=100\text{--}800$  AU) and most massive ( $M_{gas}=10^{-5}\text{--}10^{-3} M_\odot$ ,  $M_{dust+gas}=0.005\text{--}0.04 M_\odot$ ) of the disks observed in CO to date. They have been chosen to sample a range of luminosity (see  $L_*$  and  $L_X$  in Table 3.2) and dust properties, with the degree of dust settling in the disks being represented by  $L_{IR}/L_{bol}$ . In the case of DM Tau, single dish observations of CN, HCN and HNC indicate that this source is quite similar to LkCa 15. Due to its large extent ( $R_{out}=800$  AU), DM Tau will provide an excellent opportunity to examine whether the unusual CN and HCN distributions seen in LkCa 15 (c.f. Figure 4.5) are representative of large disks.

## 3.2 Observations

The observations were made using the Owens Valley Radio Observatory (OVRO) Millimeter Array at Big Pine, California between September 2002 and January 2003. The  $^{12}\text{CO}$  1-0,  $^{13}\text{CO}$  1-0 and CN  $1_{023}\text{--}0_{012}$  transitions were observed simultaneously, with a channel width of 0.33 km/s. The  $\text{HCO}^+$  1-0, HCN  $1_2\text{--}0_1$  and HNC 1-0 transitions were also acquired simultaneously at a slightly lower velocity resolution,  $\Delta v=0.42$  km/s. The sources were observed in combinations of the C and L configurations resulting in the beam sizes shown in Table 3.4. Two sources were observed in each 8 hour track (CQ Tau/MWC 758, DL Tau/DM Tau, AB Aur/RY Tau, and AA Tau/Haro 6-5 B), resulting in approximately 3 hours on source for each disk.

The bandpass was calibrated using a boxcar fit to an internal noise source modified by a second order polynomial fit to observations of an astronomical source; either 3C84, 3C454.3, 3C345, 3C279 or 3C273 were used subject to availability at the time of observation. Integrations on a phase and amplitude calibrator were interleaved with source observations approximately every half hour. The flux density scale was established from observations of the quasars noted above, with fluxes found

Table 3.3. Observed transitions

Molecule	Transition	$\nu$ (GHz)	$\Delta v$ (km/s)
CO	1-0	115.2712018	0.325
HCO <sup>+</sup>	1-0	89.1885230	0.420
CN	1 <sub>023</sub> -0 <sub>012</sub>	113.4909850	0.330
HCN	1 <sub>2</sub> -0 <sub>1</sub>	88.6318470	0.423
HNC	1-0	90.6635930	0.413

by bootstrapping from  $\sim$ concurrent observations of Neptune and Uranus. Bandpass, phase and flux calibrations were applied to the data with the MMA software package (Scoville et al., 1993). Subsequent imaging and spectral analysis were performed using the MIRIAD data reduction software package (Sault et al., 1995).

### 3.3 Column densities

It is convenient to describe the observed intensities, given in Jy ( $= 10^{-26} \text{ Wm}^{-2}\text{Hz}^{-1}$ ), in terms of the brightness temperature  $T_B$  of a blackbody exhibiting the observed specific intensity  $B_\nu$  at frequency  $\nu$ ,

$$B_\nu = \frac{2\nu^3/c^2}{\exp(h\nu/kT_B) - 1}, \quad (3.1)$$

where  $c$  is the speed of light in units of m/s and  $k$  is the Boltzmann constant in units of J/K. In the Raleigh-Jeans limit,  $h\nu \ll kT$ , which is appropriate for millimeter observations, the exponential term can be approximated by  $[\exp(h\nu/kT_B) - 1] \approx h\nu/kT_B$  and the blackbody intensity becomes

$$B_\nu = \frac{2\nu^2}{c^2} kT_B. \quad (3.2)$$

By summing the intensity  $B_\nu$  [ $\text{Jy}/\text{beam} = 10^{-26} \text{ Wm}^{-2}\text{Hz}^{-1}\text{sr}^{-1}$ ] over the source and normalizing by the shape of the synthesized beam, we then obtain a spectrum, which is the total flux over the chosen aperture for each channel in units of spectral flux density [ $\text{Jy} = 10^{-26} \text{ Wm}^{-2}\text{Hz}^{-1}$ ],

$$S_\nu[\text{Jy}] = \frac{\int B_\nu[\text{Jy}/\text{bm}] d\Omega_{bm}}{\int d\Omega_{bm}}. \quad (3.3)$$

To obtain the average brightness temperature over the source, one must divide by the solid angle  $\Delta\Omega_A$  [ $\text{sr}^{-1}$ ] over which the summation was performed,

$$\Delta\Omega_A = \frac{(\theta_a \times \theta_b)}{(2\sqrt{2\ln 2})^2 (206265)^2}, \quad (3.4)$$

where  $\theta_a$  and  $\theta_b$  are the FWHM of the aperture in arcseconds and 206265 is the conversion factor for arcseconds to radians. The Raleigh-Jeans brightness temperature in Kelvin averaged over the source can thus be calculated via the equation,

$$T_B = \frac{S_\nu}{k} \frac{1}{\Delta\Omega_A} \frac{c^2}{2\nu^2} \quad (3.5)$$

$$= \frac{S_\nu [Jy] 10^{-26}}{1.38 \times 10^{-23} J/K} \frac{(2\sqrt{2\ln 2})^2 (206265)^2 (2.99 \times 10^8 m/s)^2}{(\theta_a \times \theta_b) 2(\nu [GHz] 10^9)^2} \quad (3.6)$$

$$= 7.68 \times 10^6 \frac{S_\nu [Jy]}{(\theta_a \times \theta_b) \nu [GHz]^2}. \quad (3.7)$$

The observed intensity is more accurately represented by the antenna temperature  $T_A^*$ , which takes the instrumental efficiency  $\eta$  into account,  $T_A^* = \eta T_B$ , and is defined as the temperature required by a resistor to generate the observed power density at frequency  $\nu$ .

Gaussian fits to the observed emission lines were used to obtain the integrated intensities ( $\int T_A^* dv$ ) in units of K km/s, shown in Table 3.4.

$$\int A_0 e^{-(z^2/2\sigma^2)} dz = A_0 \sqrt{2\pi\sigma^2} = 1.064 A_0 FWHM \quad (3.8)$$

where  $A_0$  is the peak of the Gaussian,  $z = v - v_0$  and  $dz = dv$ . If emission was not detected, the rms noise level obtained in the observation (Table 3.4) was used to calculate an upper limit for the integrated intensity by integrating over a Gaussian with a peak flux of  $3\sigma$  and a base width (at  $1\sigma$ ) equal to that of the CO 1-0 transition toward the same source. In all cases, the total column densities were then calculated from the integrated intensities using the following relation, assuming that the emission is optically thin,

$$\int T_A^* dv = \frac{8\pi^3}{3k} \nu \mu^2 S \frac{N_T}{Q(T_{ex})} e^{-E_u/kT_{ex}}. \quad (3.9)$$

Here  $S$  is the line strength and is obtained from integrated intensities ( $I_{cat}$ ) of the emission lines in laboratory spectra obtained at a temperature ( $T_0 = 300K$ ) as reported in the JPL Molecular Spectroscopy on-line catalog (Pickett et al., 1998) via the relationship,

$$I_{cat} = \frac{8\pi}{3k} \mu^2 S Q(T_0) \left\langle e^{-E_l/kT_0} - e^{-E_u/kT_0} \right\rangle. \quad (3.10)$$

In the two equations above,  $N_T$  is the column density in  $cm^{-2}$ ,  $Q(T)$  is the rotational partition function at temperature  $T$ ,  $E_u$  and  $E_l$  are the energies (in ergs) of the upper and lower states,  $\nu$  is the transition frequency (Hz),  $\mu$  is the permanent dipole moment and  $k$  is the Boltzmann constant.

In addition, it was assumed that the emitting region is in Local Thermal Equilibrium (LTE) and is roughly isothermal with a temperature of  $T_K = T_{ex} = 30$  K. The use of LTE may not be the

Table 3.4. Molecular line observations: Intensities and column densities

Source	Transition	$\theta_{syn}$ (arcsec)	$v_{LSR}$ (km/s)	$\Delta v$ (km/s)	Int. Inten (K km/s)	N (30 K) ( $\text{cm}^{-2}$ )	SNR
AA Tau	CO 1-0	5.64×4.21	6.3	5.1	13.0	$2.09\pm 0.58\times 10^{16}$	3.6
	CN 1 <sub>023</sub> -0 <sub>012</sub>	5.28×5.05	...	...	13.6	$< 3.89\times 10^{14}$	...
	HCN 1 <sub>2</sub> -0 <sub>1</sub>	8.62×7.58	...	...	4.36	$< 2.74\times 10^{13}$	...
	HCO <sup>+</sup> 1-0	8.82×7.05	6.5	3.8	4.75	$1.40\pm 0.50\times 10^{13}$	2.8
	HNC 1-0	8.29×7.78	6.4	5.1	3.52	$1.14\pm 0.29\times 10^{13}$	3.9
AB Aur	CO 1-0	5.57×4.36	5.7	2.6	248	$3.99\pm 0.11\times 10^{17}$	37
	CN 1 <sub>023</sub> -0 <sub>012</sub>	6.18×4.95	6.5	8.0	38.5	$5.29\pm 0.40\times 10^{14}$	17
	HCN 1 <sub>2</sub> -0 <sub>1</sub>	7.18×5.77	...	...	...	$< 6.27\times 10^{12}$	...
	HCO <sup>+</sup> 1-0	7.28×5.57	5.0	3.6	5.64	$1.67\pm 0.39\times 10^{13}$	4.3
	HNC 1-0	7.30×5.91	...	...	...	$< 1.39\times 10^{13}$	...
CQ Tau	CO 1-0	6.37×4.76	6.1	5.7	8.05	$1.29\pm 0.36\times 10^{16}$	3.6
	CN 1 <sub>023</sub> -0 <sub>012</sub>	6.80×5.98	...	...	...	$< 6.26\times 10^{14}$	...
	HCN 1 <sub>2</sub> -0 <sub>1</sub>	6.51×4.75	4.0	7.0	7.41	$4.65\pm 1.6\times 10^{13}$	2.8
	HCO <sup>+</sup> 1-0	6.71×4.55	5.5	7.0	7.66	$2.27\pm 0.28\times 10^{13}$	8.2
	HNC 1-0	6.78×4.79	...	...	...	$< 7.37\times 10^{13}$	...
DM Tau	CO 1-0	6.59×6.07	6.1	1.4	10.9	$1.76\pm 0.11\times 10^{16}$	16
	CN 1 <sub>023</sub> -0 <sub>012</sub>	7.19×6.03	...	...	...	$< 1.30\times 10^{14}$	...
	HCN 1 <sub>2</sub> -0 <sub>1</sub>	5.94×4.23	...	...	...	$< 4.58\times 10^{13}$	...
	HCO <sup>+</sup> 1-0	6.08×4.13	5.6	3.9	14.0	$4.14\pm 0.82\times 10^{13}$	5.0
	HNC 1-0	6.31×4.20	...	...	...	$< 2.36\times 10^{13}$	...
FS Tau	CO 1-0	5.44×4.17	8.6	1.3	26.0	$4.19\pm 0.22\times 10^{16}$	19
	HCO <sup>+</sup> 1-0	8.68×7.02	7.5	3.8	4.81	$1.42\pm 0.31\times 10^{13}$	4.6
Haro 6-5B	CO 1-0	5.44×4.17	8.1	0.64	13.3	$2.13\pm 0.08\times 10^{16}$	24
	CN 1 <sub>023</sub> -0 <sub>012</sub>	5.15×4.92	...	...	...	$< 2.29\times 10^{14}$	...
	HCN 1 <sub>2</sub> -0 <sub>1</sub>	8.56×7.55	7.8	1.2	1.07	$6.71\pm 1.8\times 10^{12}$	3.8
	HCO <sup>+</sup> 1-0	8.68×7.02	8.6	1.4	3.08	$9.12\pm 2.3\times 10^{12}$	4.0
	HNC 1-0	8.22×7.66	...	...	...	$< 3.83\times 10^{12}$	...
MWC 758	CO 1-0	6.59×5.28	5.5	2.6	7.10	$1.14\pm 0.11\times 10^{16}$	10
	CN 1 <sub>023</sub> -0 <sub>012</sub>	6.73×5.97	...	...	...	$< 2.46\times 10^{14}$	...
	HCN 1 <sub>2</sub> -0 <sub>1</sub>	6.49×4.74	...	...	...	$< 7.05\times 10^{13}$	...
	HCO <sup>+</sup> 1-0	6.59×4.56	...	...	...	$< 2.62\times 10^{13}$	...
	HNC 1-0	6.66×4.77	...	...	...	$< 3.57\times 10^{13}$	...
RY Tau	CO 1-0	5.47×4.31	8.8	7.5	5.71	$9.18\pm 1.2\times 10^{15}$	7.5
	CN 1 <sub>023</sub> -0 <sub>012</sub>	6.22×4.91	10.7724	0.73386	2.44	$6.99\pm 2.3\times 10^{13}$	3.0
	HCN 1 <sub>2</sub> -0 <sub>1</sub>	7.08×5.88	8.0	8.0	5.94	$3.73\pm 1.4\times 10^{13}$	2.7
	HCO <sup>+</sup> 1-0	7.16×5.68	...	...	...	$< 4.78\times 10^{13}$	...
	HNC 1-0	7.26×6.01	...	...	...	$< 4.12\times 10^{13}$	...

Table 3.5. Summary of the 2.7 mm continuum results

Source	$\alpha$ (hms)	$\delta$ (dms)	$R_{FWHM}$ (AU)	$F_\nu$ (mJy)	$M_D$ ( $M_\odot$ )	$M_{D+G}$ ( $M_\odot$ )
AA Tau	4:34:55.426	24:28:53.105	$<993\pm 9$	$5.35\pm 0.12$	5.89e-4	0.0589
AB Aur	4:55:45.841	30:33:04.693	$<653\pm 5$	$7.63\pm 0.29$	1.10e-3	0.110
CQ Tau	5:35:58.498	24:44:54.318	$<692\pm 2$	$19.6\pm 0.18$	1.10e-3	0.110
DM Tau	4:33:48.767	18:10:09.774	$<522\pm 3$	$14.4\pm 0.37$	1.59e-3	0.159
Haro 6-5B	4:22:00.703	26:57:32.665	$<273.3\pm 0.6$	$11.0\pm 0.30$	1.21e-3	0.121
MWC 758	5:30:27.507	25:19:57.133	$<1680\pm 30$	$6.33\pm 0.27$	1.42e-3	0.142
RY Tau	4:21:57.415	28:26:35.657	$<876.9\pm 0.8$	$26.3\pm 0.40$	2.62e-3	0.262

best assumption as most of the emission is thought to arise near the superheated disk surface (van Zadelhoff et al., 2001), and a more detailed, non-LTE analysis is being pursued in a separate study. An isothermal disk with temperature 30 K is appropriate for the outer radii ( $> 70$  AU) of the disks to which we are sensitive at millimeter wavelengths (D’Alessio et al., 1999). The resulting column densities and  $3\sigma$  upper limits are presented in Table 3.4. Future work will involve more detailed models of the molecular emission using the computational tools outlined in Chapter 2.

### 3.4 Continuum and $^{12}\text{CO}$ observations

Maps of the continuum and  $^{12}\text{CO}$  1-0 emission are shown in Figure 3.1. In the left column, the continuum is shown in color scale and the integrated intensity of the  $^{12}\text{CO}$  1-0 is overplotted with contours. The velocity structure of the  $^{12}\text{CO}$  1-0 emission is shown in color scale in the right column. It is evident from these images that the 2.7 mm continuum traces a much smaller portion of the disk than does emission from the CO gas. Similarly, we find that the continuum emission is unresolved toward most of the sources in our sample and constrain the size of the 2.7 mm continuum as shown in Table 3.5. This can be attributed to the rapid decrease in dust emissivity as a function of wavelength, and is not likely due to an absence of small grains at large radii (Sargent & Beckwith, 1987; Lay, 1997; Qi et al., 2003). The CO 1-0 emission is resolved and the FWHM sizes of the disks in our sample are listed in Table 3.6.

The total disk masses  $M_{gas+dust}$  are calculated from the continuum flux densities using the approach of Beckwith et al. (1990). The flux density is defined as

$$F_\nu = \int I_\nu d\Omega = \int S_\nu \tau_\nu d\Omega, \quad (3.11)$$

where  $\tau$  is the dust optical depth. We have assumed that the dust is optically thin, which is a fair assumption for wavelengths longer than  $300 \mu\text{m}$ . Typical dust temperatures,  $T_D$ , are high enough

Table 3.6.  $^{12}\text{CO}$  1-0 observations

Source	$\theta_{bm}$ (arcsec)	$\text{PA}_{bm}$ (deg)	$v_{LSR}$ (km/s)	$R_{FWHM}^a$ (AU)	$\text{PA}^a$ (deg)	$i^b$ (deg)	$M_{H_2}$ ( $M_{\odot}$ )
AA Tau	$5.64 \times 4.21$	-85.4	6.3	$1130 \pm 60 \times 860 \pm 30$	$-88.7 \pm 0.7$	40	$1.07 \times 10^{-4}$
AB Aur	$5.57 \times 4.36$	-54.4	5.7	$1549 \pm 4 \times 1088 \pm 2$	$54.40 \pm 0.08$	45	$3.81 \times 10^{-3}$
CQ Tau	$6.37 \times 4.76$	-86.1	6.1	$560 \pm 20 \times 380 \pm 10$	$86.4 \pm 0.5$	47	$1.61 \times 10^{-5}$
DM Tau	$6.59 \times 6.07$	-29.5	6.1	$1076 \pm 8 \times 683 \pm 4$	$-8.6 \pm 0.1$	51	$8.12 \times 10^{-5}$
Haro 6-5B	$5.44 \times 4.17$	-86.2	8.1	$910 \pm 10 \times 564 \pm 6$	$-77.4 \pm 0.1$	52	$7.03 \times 10^{-5}$
MWC 758	$6.59 \times 5.28$	-72.9	5.5	$< 1800 \pm 10$	...	...	$1.47 \times 10^{-4}$
RY Tau	$5.47 \times 4.31$	-53.1	8.8	$650 \pm 50 \times 300 \pm 20$	$74 \pm 2$	62	$1.54 \times 10^{-5}$

<sup>a</sup>This is the deconvolved source size and position angle.

<sup>b</sup>The inclinations calculated here largely follow the beam ellipticity. Calculations of  $i$  via comparison with models (i.e., using the method described in Chapter 2) are more reliable and will be performed in the near future.

( $T_D > 50K$ ) to make the Rayleigh-Jeans assumption valid;

$$S_{\nu} \approx B_{\nu} = 2kT \frac{\nu^2}{c^2}. \quad (3.12)$$

Using the definitions of optical depth ( $\tau = \kappa_{\nu} \Sigma$ ) and solid angle ( $\Omega = \frac{\sigma}{D^2}$ ), the flux density  $F_{\nu}$  can then be related to the dust mass ( $M_D = \int \Sigma d\sigma$ ) via the equation,

$$F_{\nu} \approx \int 2kT \frac{\nu^2}{c^2} \kappa_{\nu} \Sigma d\frac{\sigma}{D^2} = \frac{2k \langle T \rangle \nu^2}{D^2 c^2} \kappa_{\nu} M, \quad (3.13)$$

where  $\kappa_{\nu}$  is the mass opacity,  $\Sigma$  is the surface density,  $\sigma$  is the surface area of the disk and  $D$  is the distance to the disk. The total emission is proportional to a product of the total mass and the average temperature  $\langle T \rangle$ , weighted appropriately by its radial distribution. The major uncertainty in the mass estimates arises from  $\kappa_{\nu}$ . Theoretically,  $\kappa_{\nu}$  is expected to vary as a power of the frequency  $\nu$ :  $\kappa_{\nu} = \kappa_0 \left(\frac{\nu}{\nu_0}\right)^{\beta}$ . Following Beckwith et al. (1990), we adopt a fiducial value of 0.02 ( $\frac{\nu}{230\text{GHz}}$ )  $\text{cm}^2 \text{g}^{-1}$  and calculate the total gas mass assuming  $M_{gas}/M_{dust} = 100$ .

The disk gas mass  $M_G$  can also be calculated from the CO 1-0 observations, using the column density calculated above, following Scoville et al. (1986),

$$M_{H_2} = N_{CO} \mu_G m_{H_2} \frac{\pi \theta^2}{4} D^2. \quad (3.14)$$

In this equation,  $\mu_G = 1.36$  is the mean atomic weight of the gas,  $m_{H_2} = 3.345 \times 10^{-24}$  g is the mass of one  $\text{H}_2$  molecule, and  $\theta$  is the angular diameter (FWHM) of the uniform disk source. For the standard CO fractional abundance,  $N_{H_2}/N_{CO} \approx 10^4$ , we obtain a lower limit to the gas masses

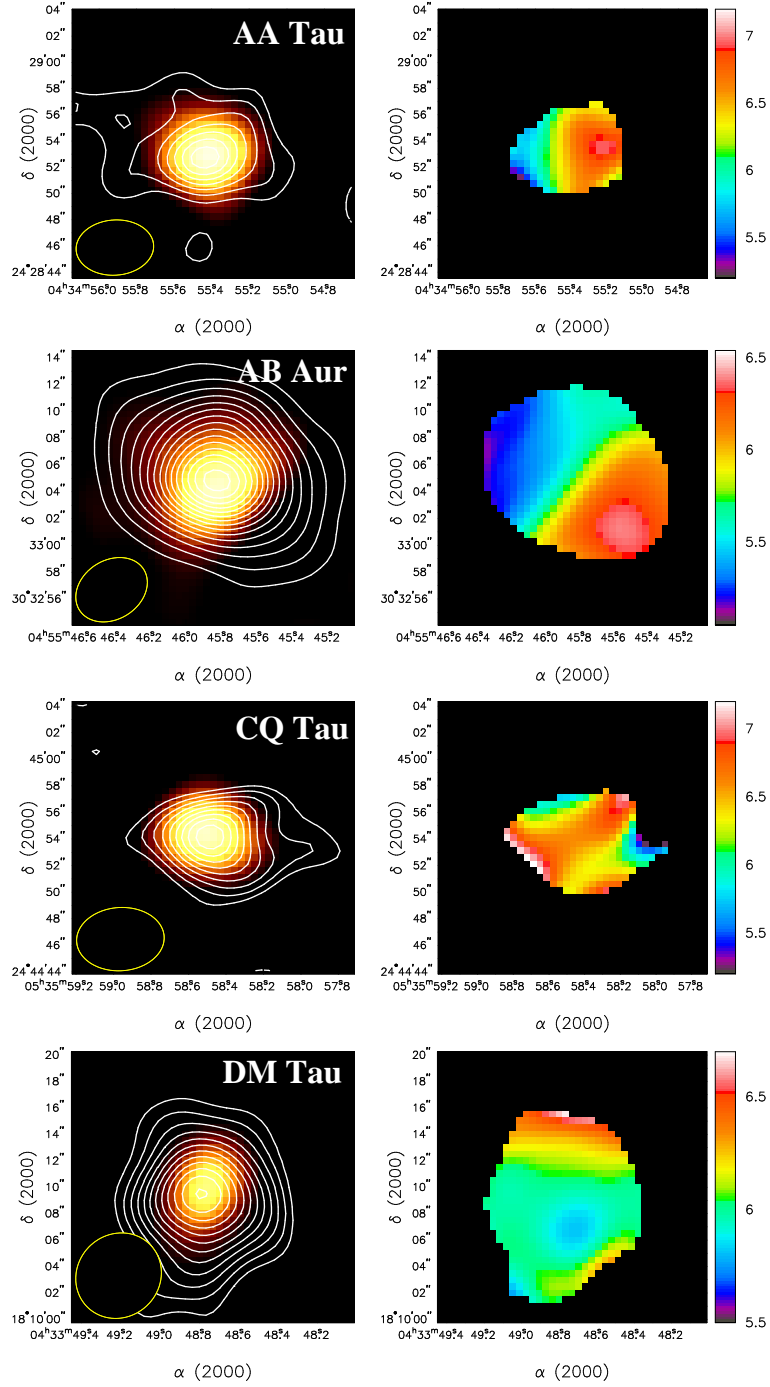


Figure 3.1 Maps of the continuum and CO 1-0 emission toward the sample. The left panel shows the continuum (color scale) and CO 1-0 integrated intensity maps (contours). Contours start at  $2\sigma$  for AA Tau, AB Aur and DM Tau and at  $1\sigma$  for CQ Tau, Haro 6-5B, MWC 758 and RY Tau. The right panel shows the CO 1-0 velocity maps, starting at  $3\sigma$  for all sources.

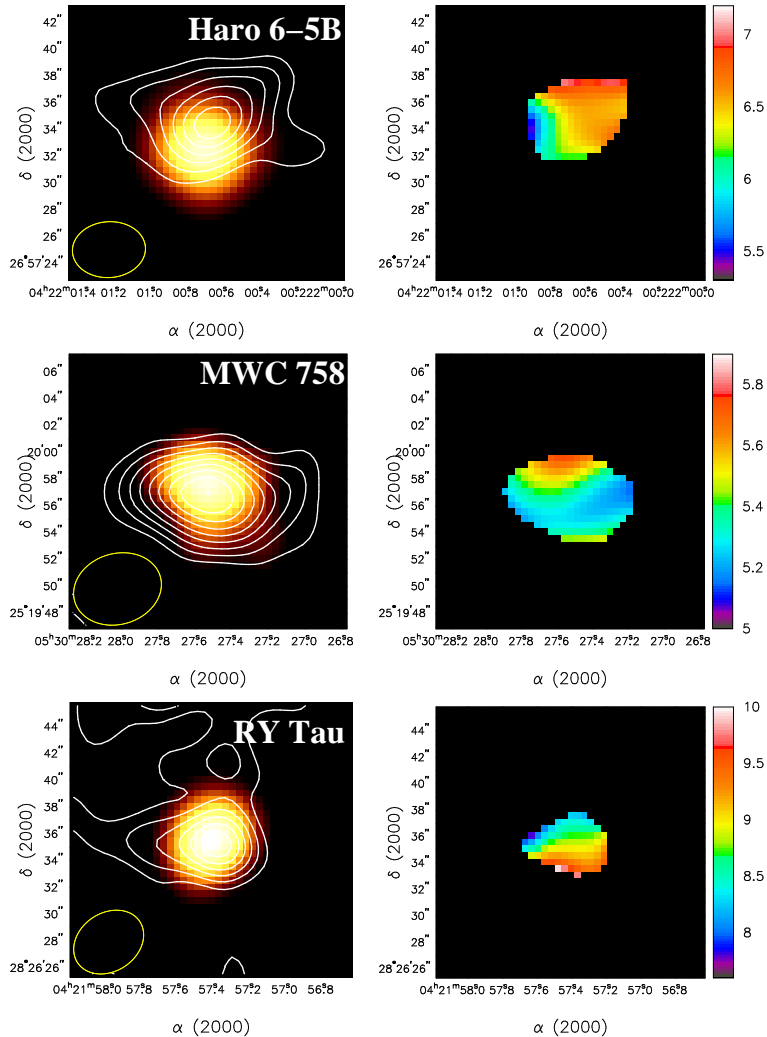


Figure 3.1 -continued.

presented in Table 3.6. Although the gas masses calculated in this way are reasonably consistent with previous observations, the dust masses are consistently too small, perhaps due to low interferometer sensitivity at large radii as discussed above, especially for the short integration times used.

### 3.5 $\text{HCO}^+/\text{CO}$ and ionization

The degree of ionization is important because it affects both the physical and chemical structure of disks. Stellar accretion and molecular outflows occur along magnetic field lines and the slowing of disk and stellar rotation are therefore believed to be strongly influenced by magneto-hydrodynamic processes. Radiative and vertical transport in the outer disk also likely depend on the degree of ionization, with coupling between the neutral and magnetic fields occurring at fractional ionizations of  $\geq 10^{-8}$  (Feigelson & Montmerle, 1999). The chemical complexity within disks is also stimulated

by ionization. Ion-molecule reactions proceed much more quickly than neutral-neutral reactions, as ions induce dipoles in their collision partners, thus increasing collision rates;  $k_c \sim 10^{-11}$  cm<sup>3</sup>/s for neutral-neutral reactions while  $k_c \sim 10^{-9}$  cm<sup>3</sup>/s for ion-molecule reactions. Because H<sub>2</sub> is very abundant in disks, the formation rate of H<sub>2</sub><sup>+</sup> is equal to the ionization rate of the disk. For the same reason, H<sub>2</sub><sup>+</sup> once formed reacts quickly with additional H<sub>2</sub> to form H<sub>3</sub><sup>+</sup>. Due to the efficiency of charge transfer reactions, the charge and degree of protonation spreads quickly to other molecules (and atoms) and the protonation of C and O by H<sub>3</sub><sup>+</sup> is a vital step in the production of carbon chains and prebiotic molecules.

In the dense and cold disk midplane, extensive molecular depletion ensures that H<sub>3</sub><sup>+</sup> is the dominant gas-phase cation. H<sub>3</sub><sup>+</sup> is unobservable at millimeter wavelengths, but fortunately near the disk surface CO is the most abundant molecule after H<sub>2</sub> and carries much of the charge as HCO<sup>+</sup>. HCO<sup>+</sup> is produced and destroyed via the mechanism



The charge transfer reactions producing H<sub>2</sub><sup>+</sup>, H<sub>3</sub><sup>+</sup> and HCO<sup>+</sup> proceed at the Langevin rate ( $\sim 10^{-9}$  cm<sup>3</sup> s<sup>-1</sup>), but the dissociative recombination reactions are also efficient ( $\sim 10^{-7}$  cm<sup>3</sup> s<sup>-1</sup>) and it can be assumed that the system is in steady state and the abundances of H<sub>2</sub><sup>+</sup>, H<sub>3</sub><sup>+</sup> and HCO<sup>+</sup> remain fairly constant with time. Therefore,

$$\frac{d[H_2^+]}{dt} = 0 = \zeta[H_2] - k_{3.16}[H_2^+][H] \quad (3.20)$$

$$\frac{d[H_3^+]}{dt} = 0 = k_{3.16}[H_2^+][H_2] - k_{3.18}[H_3^+][e] - k_{3.17}[CO][H_3^+] \quad (3.21)$$

$$\frac{d[HCO^+]}{dt} = 0 = k_{3.17}[CO][H_3^+] - k_{3.19}[HCO^+][e]. \quad (3.22)$$

In the equations above, the bracket [ ] represents the fractional abundance of the species and  $\zeta$  is the ionization rate due to cosmic rays, x-rays and UV radiation. Rate constants for the reactions above  $k_{3.16} - k_{3.19}$  are taken from the UMIST database for astrochemistry and are presented in Table 3.7. As discussed above, H<sub>3</sub><sup>+</sup> is very abundant in disks so that  $[H_3^+]/[HCO^+] > 1$  and solution of equation 3.22 gives an upper bound to the electron abundance [e];

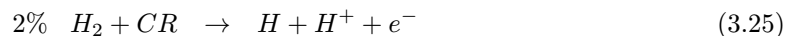
$$\frac{[e]}{[CO]} < \frac{k_{3.17}}{k_{3.19}}. \quad (3.23)$$

Table 3.7. Relevant reactions and rate coefficients,  $k_r = \alpha (T/300)^{-\beta}$ . Rate coefficients are from the UMIST database (Millar et al., 1997).

R1	R2	P1	P2	$\alpha$	$\beta$
$\text{H}_2^+$	$\text{H}_2$	$\text{H}_3^+$	$\text{H}$	$2.08 \times 10^{-9}$	0.0
$\text{H}_3^+$	$\text{CO}$	$\text{HCO}^+$	$\text{H}_2$	$6.56 \times 10^{-10}$	0.5
$\text{H}_3^+$	$e^-$	$\text{H}$	$\text{H}_2$	$1.15 \times 10^{-7}$	0.65
$\text{HCO}^+$	$e^-$	$\text{CO}$	$\text{H}$	$2.00 \times 10^{-7}$	0.75

This results in an upper limit for the fractional ionization ( $[e]/[\text{H}_2]$ ) of  $\sim 10^{-8}$ , with an assumed  $\text{H}_2$  column density of  $N_{\text{H}_2} = 10^5 N_{\text{CO}}$  (Qi et al., 2003).

Although we cannot use the observed  $\text{HCO}^+$  abundances alone to establish the electron abundance, we can estimate the fractional ionization from our understanding of the ionization rates due to cosmic rays, X-rays and radioactive decay. The degree of ionization depends largely on the effectiveness of cosmic ray ionization of He and  $\text{H}_2$  through the following reactions (Duley & Williams, 1984):



Nakano & Tademaru (1972) perform detailed calculations of cosmic ray ionization rates and find that the rate of ionization is  $\zeta_{\text{CR}} = 6.1 \times 10^{-18} \exp(-x/r) \text{ s}^{-1}$ , where  $r = 66 \text{ g/cm}^2$ , and  $x$  is a measure of the surface density at depth  $h$  into the disk, defined by  $x = \rho h$ . Using this method they find that cosmic rays are quenched when the surface density approaches  $x=96 \text{ g/cm}^3$ . This is much higher than the surface density of the outer disk, and thus cosmic rays are believed to be largely unattenuated in disks and a standard value of  $\zeta_{\text{CR}} = 1.3 \times 10^{-17} \text{ s}^{-1}$  per H atom is often used for the cosmic ray ionization rate beyond  $\sim 30 \text{ AU}$  (Umebayashi & Nakano, 1981; Aikawa et al., 2002).

Nakano & Tademaru (1972) also calculate the ionization rate due to hard ( $E > 1 \text{ keV}$ ) X-rays, via the relation,

$$\zeta_x = 1.9 \times 10^{-23} x^{-1.23} \text{ s}^{-1}, \quad (3.28)$$

and find that  $\zeta_x$  in disks is negligible compared to cosmic rays at depths beyond the very surface of disks,  $x < 0.03 \text{ g cm}^{-3}$ . However, they do not consider the effects of secondary electrons in their calculation of the ionization rate. Upon inclusion of secondary electrons, Igea & Glassgold (1999) find that even at low stellar X-ray luminosities,  $10^{29} \text{ erg s}^{-1}$ , hard X-rays are important in the ionization

Table 3.8. HCO<sup>+</sup> Observations and estimated ionization rates and fractional ionization

Source	HCO <sup>+</sup> /CO	R	$\zeta_X$	$n_i/n_H(0)$	$n_i/n_H(\text{IG})$
AA Tau	$6.7 \pm 3.1 \times 10^{-4}$	100	$1 \times 10^{-15}$	$7.63 \times 10^{-9}$	$1 \times 10^{-6}$
AB Aur	$4.2 \pm 0.97 \times 10^{-5}$	250	$2 \times 10^{-16}$	$6.69 \times 10^{-9}$	$2 \times 10^{-7}$
CQ Tau	$1.7 \pm 0.53 \times 10^{-3}$	67	$7 \times 10^{-16a}$	$4.47 \times 10^{-9}$	$5 \times 10^{-7}$
DM Tau	$2.3 \pm 0.5 \times 10^{-3}$	425	$8 \times 10^{-17}$	$1.86 \times 10^{-8}$	$4 \times 10^{-7}$
Haro 6-5B	$4.3 \pm 1.1 \times 10^{-4}$	100	$3 \times 10^{-16a}$	$2.12 \times 10^{-8}$	$1 \times 10^{-6}$
MWC 758	$< 2.3 \times 10^{-3}$	117	$2 \times 10^{-16a}$	$4.88 \times 10^{-9}$	$2 \times 10^{-7}$
RY Tau	$< 5.2 \times 10^{-3}$	78	$2 \times 10^{-15}$	$4.54 \times 10^{-9}$	$1 \times 10^{-6}$

<sup>a</sup> $L_X$  has not been measured for these sources, so  $\log(L_X) = 29$  was assumed.

of disk material, penetrating deeper than Galactic cosmic rays and producing large ionization rates ( $\zeta$  up to  $10^{-12} \text{ s}^{-1}$  at  $R=1 \text{ AU}$ ). The vertical penetration depth of the X-rays ( $\sim 10^{25} \text{ cm}^{-2}$ ) is comparable with the thickness of the disk at moderate radial distances ( $R \sim 1-10 \text{ AU}$ , depending on disk mass). Igea & Glassgold (1999) perform a full 3D calculation of X-ray transport and ionization in axially symmetric disks using a Monte Carlo method and find that the X-ray ionization rate is largely independent of disk surface density and mass and proportional to X-ray luminosity ( $\zeta_x \propto L_X$ ) and to the inverse square of the disk radius ( $\zeta_x \propto R^{-2}$ ) for any particular vertical column density. Since these models are calculated for  $L_X = 10^{29} \text{ erg s}^{-1}$  and  $R = 1 \text{ AU}$ , the ionization rate for any X-ray luminosity and radius can be represented by

$$\zeta_x = \zeta_{IG}(N_T) \left( \frac{L_X}{10^{29} \text{ ergs}^{-1}} \right) \left( \frac{R}{1 \text{ AU}} \right)^{-2}, \quad (3.29)$$

where  $\zeta_{IG}(N_T)$  is the ionization rate from Igea & Glassgold (1999), at the appropriate vertical column density ( $N_T$ ). The X-ray ionization rates for the disks in our sample have been calculated in this manner and are shown in Table 3.8. Because molecular line emission from low-lying J states has been proven to arise from a warm layer near disk surfaces (van Zadelhoff et al., 2001; Qi et al., 2003), we assume that our observations probe such a layer and use  $\zeta_{IG}(N_T) \approx 3 \times 10^{-12}$ , the value at the disk surface at  $R = 1 \text{ AU}$ . This is then scaled via the equation above to an appropriate radius depending on the disk size. The resulting X-ray ionization rates are much higher than the canonical value of  $\sim 10^{-20} \text{ s}^{-1}$ , obtained via equation 3.28 using  $x = 0.003 \text{ g cm}^{-2}$  for a depth of 50 AU, which corresponds to a density of  $n_H = 10^6 \text{ cm}^{-3}$  in a typical disk. In fact, the X-ray ionization rates calculated here are larger than the Galactic cosmic ray ionization rate ( $\zeta_{CR} = 2 \times 10^{-17} \text{ s}^{-1}$ ). Thus, hard X-ray emission from the central star is an important contributor to the ionization rate near the disk surface. This may additionally be enhanced by soft X-rays from the central star, although such

low energy X-rays would likely be absorbed by any outflow activity near the stellar surface (Igea & Glassgold, 1999).

The effect of the increase in the X-ray ionization on the total fractional ionization can be calculated by evaluating the mechanisms for production and destruction of ions within the disk (see Nakano & Tademaru, 1972). We will consider the production of ions via cosmic ray ionization, using the methods of Nakano & Tademaru (1972) to calculate the cosmic ray ionization rates ( $\zeta_{CR} = 6.1 \times 10^{-18} \exp(-x/66) \text{ s}^{-1}$ ) near the disk surface ( $x = 0.007$  as above), and the production of ions via X-ray ionization using the rates calculated above by scaling the results of Igea & Glassgold (1999). Radioactive decay (of  $^{26}\text{Al}$ , for example,  $\zeta_R = 6 \times 10^{-18} \text{ s}^{-1}$ , Umebayashi & Nakano, 1981) may also play an important role in ionization in disks, particularly near the disk midplane and so is also included. Ions can be destroyed through recombination on grain surfaces or radiative recombination (rate =  $\sigma_g v_s (n_g/n_H)$ ) in the gas phase ( $2.08 \times 10^{-11} \text{ T}^{-1/2} 0.5 n_e$ ). Assuming equilibrium between ionization and recombination, the number of ions can be calculated using the equation,

$$n_i = \frac{\zeta_{CR}(x) + \zeta_R + \zeta_x(x)}{\sigma_g c_s \frac{n_g}{n_H} + 2.08 \times 10^{-11} T^{-1/2} \phi n_e}. \quad (3.30)$$

The grain cross-sectional area and the fractional abundance of grains are fixed at  $\sigma_g = 7 \times 10^{-10} \text{ cm}^2$  and  $n_g/n_H = 10^{-12}$ . The product  $\sigma_g n_g \approx 7 \times 10^{-22}$  can be assumed to be constant as grains coagulate and grow. The sound speed,  $c_s = (H/R) \times \sqrt{GM_{cent}/R}$ , is approximately the relative velocity of ions and grains, and is calculated using an aspect ratio  $(H/R) \sim 0.12$ , typical of circumstellar disks (i.e., D'Alessio et al., 2001) at the radii probed by our observations, as indicated in Table 3.8. Radiative recombination is proportional to  $n_i^2$ , so as  $n_i$  decreases, this process becomes less important relative to recombination on grain surfaces, and can be ignored for  $n_i/n_H < 10^{-5}$  (Nakano & Tademaru, 1972). Therefore, we consider only the effects of grain surface recombination.

Using the method described above, we calculate the ionization fraction at the appropriate radii in each disk, both with the standard X-ray ionization rate calculated by Nakano & Tademaru (1972) and the increased X-ray ionization rates from Igea & Glassgold (1999). The resulting ionization fractions, shown in Table 3.8, are larger by a factor of  $10^{2-3}$  when  $\zeta_x(IG)$  is used. From these calculations it can be seen that the inclusion of ionization by the secondary electrons produced from X-rays can have a large impact on the ionization rate in the outer regions of disks.

### 3.6 Nitrogen chemistry: CN, HCN and HNC

As discussed above, protonation of atomic carbon and oxygen by  $\text{H}_3^+$  initiates the production of most C- and O-bearing molecules, when starting with largely atomic gas. However, because the

protonation of N by  $H_3^+$  is endothermic and the reaction



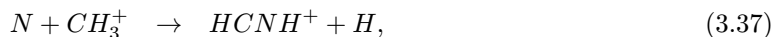
possesses a significant activation energy (Herbst et al., 1987), nitrogen atoms are expected to be more abundant than ionized nitrogen, resulting in a very different chemistry than that of O and C (as described by Pineau des Forets et al. (1990) and shown in Figure 3.2). The production of  $N_2$  occurs via the following radical-radical reactions:



with reaction 3.33 proceeding at a temperature-dependent rate of  $8.2 \times 10^{-11} \exp(-410/T) \text{ cm}^3/\text{s}$  (Prasad & Huntress, 1980) or a rate of  $3.4 \times 10^{-11} \text{ cm}^3/\text{s}$  at  $200 \leq T \leq 400 \text{ K}$  (Langer & Graedel, 1989). Subsequent ionization or protonation of NO and  $N_2$  leads to the production of  $NH_3$  and  $N_2H^+$ , which are frequently observed in molecular clouds. Alternately, atomic nitrogen may react with CH and  $CH_2$  to form CN and HCN,



Rates of  $k_{3.34} = 2.1 \times 10^{-11} \text{ cm}^3/\text{s}$  (at  $T = 298 \text{ K}$ ; Smith 1988) and  $k_{3.35} = 2.0 \times 10^{-11} (T/300\text{K})^{1/2} \text{ cm}^3/\text{s}$  (Prasad & Huntress, 1980) have been measured in the laboratory for these reactions, although abundances of  $NH_3$ , CN and HCN in molecular clouds are best reproduced by introducing a small barrier to these rate coefficients (Pineau des Forets et al., 1990). The abundances of carbon-bearing nitrogenated molecules are thus partially dependent on the C/O ratio in the gas. Ion-atom reactions also play a role in the nitrogen chemistry. The inclusion of reactions of atomic nitrogen with the methyl cation ( $k = 6.70 \times 10^{-11} \text{ cm}^3/\text{s}$ ),



rapidly leads to the production of CN and HCN through electron recombination reactions (at rates of  $1.50 \times 10^{-7} \text{ cm}^3/\text{s}$  and  $1.75 \times 10^{-7} \text{ cm}^3/\text{s}$  for CN and HCN, respectively; Figure 3.2). The primary production mechanism for HNC is believed to be dissociative recombination of  $HCNH^+$ , competing



appears to be fairly stable from source to source. In studies of 27 translucent molecular clouds, Turner et al. (1997) find a typical HNC/HCN ratio of  $\sim 0.17$ – $0.4$ , which is similar to that found for the pNe CRL 618 (HCN/HNC  $\sim 1.0$ ; Bujarrabal 1988) and for protoplanetary disks. Observations of the PDR NGC 7023 by Fuente et al., 1993, show that HNC/HCN ranges from 0.2 nearest to the star to  $\sim 1$  farthest from the stellar position. Models suggest even stronger variations with temperature and UV flux; HNC/HCN decreases by 5 orders of magnitude from  $A_V = 10$  to 6 mag at constant temperature,  $T = 30$  K, or from 15 to 50 K at constant  $A_v$  (of 10 mag). Models of PDRs suggest that HCN and HNC should both decrease with increasing kinetic temperature, because rates of reactions producing  $N_2$  and  $NH_3$  increase, reducing the supply of atomic N. In regions with larger UV fields, production of both HNC and HCN should increase due to increased production of hydrocarbons. The destruction of both HNC and HCN should also *increase* with increasing UV fields, via the reactions



Because the destruction of HNC results in the production of HCN, the HNC/HCN ratio is expected to decrease in regions with enhanced UV fields, as is indicated by the observations discussed above. However, observations of comet Hale Bopp indicate that HNC increased near perihelion (Charnley et al., 2002), which the authors explain by the reverse of reaction 3.40 driven by suprathermal H atoms produced via the UV photodissociation of water.

Fuente et al. (1993) show that the CN/HCN ratio is strongly enhanced in regions of moderate UV fields, increasing by a factor of 15 from  $A_V = 10$  mag to  $A_V = 6$  mag in PDRs, but is relatively insensitive to temperature, remaining constant from  $T = 15$ – $50$  K for  $A_V = 10$  mag. This is because increases in temperature affect the abundances of CN and HCN in the same manner, whereas HCN is much more sensitive than CN to changing UV fields. Higher temperatures lead to increases in the abundance of oxygenated molecules ( $HCO^+$ , CO,  $CO_2$ ) relative to CH,  $CH^+$  and  $C_2H$ . Thus, N atom reactions with OH lead more efficiently to  $N_2$  and  $NH_3$  than CN, HCN and HNC, proceeding off to the left in Figure 3.2, and the production of CN, HCN and HNC decreases. CN increases with increasing UV field, but decreases with increasing temperature. At low UV fields, the situation is similar, due to low abundances of C and  $C^+$ . At moderate UV fields ( $A_V = 6$ – $8$  mag with  $G_0 = 2 \times 10^3$ ), C and  $C^+$  abundances increase, stimulating hydrocarbon chemistry, and N reacts with C bearing molecules instead of OH to produce substantial amounts of CN, HCN and HNC. However, HCN and HNC are also destroyed by reaction with  $H^+$  and  $C^+$  (CN is destroyed by reaction with O and N), thus their abundances are not as high as CN in these regions. The observed enhancement in the CN/HCN ratio can therefore be explained by the decrease in the HCN abundance in regions

exposed to moderate UV fields. Additionally, the relative abundance of CN versus HCN is affected by the relative photodestruction rate of HCN (producing CN) and the photodestruction of CN itself in the presence of UV radiation. The dissociation energy of CN is higher than that of HCN, requiring photons of shorter wavelengths for dissociation,  $<1150 \text{ \AA}$  for CN (Nee & Lee, 1985) and near  $1216 \text{ \AA}$  for HCN (Nuth & Glicker, 1982). Photons of shorter wavelengths are more efficiently absorbed or scattered by dust, an effect that has also been used to explain the dominance of CN over HCN ( $\text{CN}/\text{HCN} \approx 10$ ) in planetary nebulae (Cox et al., 1992), with models of such nebulae estimating that the effective photodissociation rate of CN is smaller than that of HCN by a factor of 2–3.

It is evident from the discussion above that both the CN/HCN and HNC/HCN ratios are greatly affected by UV radiation. Due to the flared geometry of protoplanetary disks, the overall UV field of the outer disk is a combination of stellar and interstellar radiation fields (ISRF). Typical disk models assume a stellar FUV flux of  $10^4$  times higher than the ISRF at 100 AU (Willacy & Langer, 2000; Aikawa & Herbst, 2001). Radiative transfer calculations of the relative contributions of the interstellar and stellar radiation fields have been performed (van Zadelhoff et al., 2001, Aikawa et al., 2002) and find that the stellar radiation field, in particular continuum FUV radiation, is most important in disk surfaces. Using a protoplanetary disk model with a typical T Tauri star SED and stellar parameters ( $M_* = 0.5 M_\odot$ ,  $R_* = 2 M_\odot$ ,  $T_* = 4000 \text{ K}$ ,  $\dot{M} = 3 \times 10^{-8} M_\odot/\text{yr}$ ), Bergin et al. (2003) follow the transport of FUV radiation through the disk using an analytical approximation which includes both scattering and pure absorption by dust grains of sizes  $0.005 \mu\text{m} - 1 \text{ mm}$ . They find that the stellar radiation dominates over interstellar radiation in the upper 30 AU of the disk and decreases with decreasing height, becoming equally or less important than the interstellar radiation in the disk midplane largely due to the contribution of strong Lyman  $\alpha$  emission lines to the stellar FUV radiation field. These lines, however, are difficult to observe due to severe extinction by the large quantities of dust and atomic gas present in the molecular clouds in which T Tauri stars form. The impact of variations in Ly  $\alpha$  flux versus CN/HCN is therefore difficult to verify observationally.

The effective UV field in disk surface layers is also largely dependent on the attenuation by dust grains in the surface layers of the circumstellar disk. As dust grains grow, they decouple from the gas and sink to the disk midplane. Both grain growth and sedimentation enhance the effective radiation field by decreasing the total grain cross section. This then leads to increases in the photodissociation and photoionization as discussed above, likely resulting in enhanced CN to HCN abundances. Aikawa & Herbst (1999) model this decrease in dust shielding at  $R = 700 \text{ AU}$  and  $t = 3 \times 10^5 \text{ yr}$  by increasing the hydrogen column density corresponding to  $A_V = 1 \text{ mag}$  to  $1.8 \times 10^{22} \text{ cm}^2$ , an order of magnitude larger than in the standard ISM. This effectively increased the UV field and resulted in decreases in the CO, CN, HCN and HNC column densities by factors of 4.4, 2.1, 2.4 and 2.3, respectively. In contrast to the reasoning above, the CN/HCN ratio did not change significantly, although the  $\text{HCO}^+$  column density was found to increase by a factor of 2.2,

Table 3.9. Column densities of observed molecules, assuming optically thin emission in LTE.

Source	$N_T(\text{CO})^a$	$N_T(\text{HCO}^+)$	$N_T(\text{CN})$	$N_T(\text{HCN})$	$N_T(\text{HNC})$
AA Tau	$2.09 \pm 0.58 \times 10^{16}$	$1.40 \pm 0.50 \times 10^{13}$	$< 3.89 \times 10^{14}$	$< 2.74 \times 10^{13}$	$1.14 \pm 0.29 \times 10^{13}$
AB Aur	$3.99 \pm 0.11 \times 10^{17}$	$1.67 \pm 0.39 \times 10^{13}$	$5.29 \pm 0.40 \times 10^{14}$	$< 6.27 \times 10^{12}$	$< 1.39 \times 10^{13}$
CQ Tau	$1.29 \pm 0.36 \times 10^{16}$	$2.27 \pm 0.28 \times 10^{13}$	$< 6.26 \times 10^{14}$	$4.65 \pm 1.6 \times 10^{13}$	$< 7.37 \times 10^{13}$
DM Tau	$1.76 \pm 0.11 \times 10^{16}$	$4.14 \pm 0.82 \times 10^{13}$	$< 1.30 \times 10^{14}$	$< 4.58 \times 10^{13}$	$< 2.36 \times 10^{13}$
Haro 6-5B	$2.13 \pm 0.08 \times 10^{16}$	$9.12 \pm 2.3 \times 10^{12}$	$< 2.29 \times 10^{14}$	$6.71 \pm 1.8 \times 10^{12}$	$< 3.83 \times 10^{12}$
MWC 758	$1.14 \pm 0.11 \times 10^{16}$	$< 2.62 \times 10^{13}$	$< 2.46 \times 10^{14}$	$< 7.05 \times 10^{13}$	$< 3.57 \times 10^{13}$
RY Tau	$9.18 \pm 1.2 \times 10^{15}$	$< 4.78 \times 10^{13}$	$6.99 \pm 2.3 \times 10^{13}$	$3.73 \pm 1.4 \times 10^{13}$	$< 4.12 \times 10^{13}$

<sup>a</sup> $N_T(\text{CO})$  are lower limits, as it is likely that  $\tau(\text{CO}) \ll 1$  (van Zadelhoff et al., 2001); CO column densities calculated from  $^{12}\text{CO}$  and  $^{13}\text{CO}$  have been observed to differ by up to 2 orders of magnitude (Qi et al., 2003).

supporting the above scenario.

Based on the discussion above, we expect the observed CN, HCN and HNC abundances to be related to the effective stellar and interstellar radiation fields near the disk surface. In order to investigate this relationship, we search for correlations of the observed CN and HCN abundances with tracers of disk and stellar structure, including stellar luminosity (temperature), fractional IR luminosity ( $L_{\text{IR}}/L_{\text{bol}}$ ; disk flaring and optical depth), the height of the dust photosphere versus the gas scale height (dust settling) and X-ray luminosity ( $L_X$ ; ionization fraction). The results of these studies are presented in Table 3.10 and described below.

### 3.6.1 Gas temperature, stellar UV and $L_*$

The stellar luminosity  $L_*$  has an impact on disk chemistry through its effect on the temperature of the gas and through its relationship with the stellar UV field.  $L_*$  is defined as the flux  $F$  summed over the solid angle ( $\Omega$ ) subtended by the star,

$$L = \int F d\Omega = 4\pi r^2 F \quad (3.41)$$

$$F(T) = \frac{2h\nu^3/c^3}{\exp(h\nu/kT) - 1}, \quad (3.42)$$

where  $F(T)$  is the stellar blackbody flux at temperature  $T$ ,  $h$  is the Planck constant,  $k$  is the Boltzmann constant,  $c$  is the speed of light and  $\nu$  is the frequency of the radiation. At the frequencies observed here,  $\nu \sim 100$  GHz,  $h\nu/kT$  is small ( $\ll 1$ ), the Rayleigh-Jeans approximation holds and the flux is directly related to the stellar temperature [ $F(T) \approx \frac{2\nu^2}{c^2} kT$ ]. Most models indicate temperature distributions which decrease as a function of distance from the star as  $T \propto \frac{1}{\sqrt{R}}$ . For a star of  $T = 1000 - 10000$  K, the Wein law is applicable in the UV ( $h\nu \gg kT$ ), such that the stellar UV flux

Table 3.10. Abundance ratios and physical parameters.

Source	CN/CO	CN/HCN	HNC/HCN	$L_{star}$	$L_{IR}/L_{bol}$	H/h
AA Tau	$<1.9 \times 10^{-2}$	...	$>0.41$	1.5	0.15	3.8
AB Aur	$2.8 \pm 0.2 \times 10^{-3}$	$>84$	...	53.6	0.37	...
CQ Tau	$<4.8 \times 10^{-2}$	$<13$	$<0.44$	8.0	0.50	5.0
DM Tau	$<7.4 \times 10^{-3}$	...	...	0.25	0.16	...
Haro 6-5B	$<1.1 \times 10^{-2}$	$<34$	$<0.57$	...	0.02	...
MWC 758	$<2.1 \times 10^{-2}$	...	...	20.6	0.75	1.5
RY Tau	$7.6 \pm 2.7 \times 10^{-3}$	$1.9 \pm 0.9$	$<1.1$	16.7	0.65	...
LkCa 15	$2.55 \times 10^{-4}$	10.2	$<0.22$	0.724	0.11	1.0
GM Aur	$7.73 \times 10^{-5}$	1.89	...	0.741	0.11	2.0
HD 163296	$1.74 \times 10^{-4}$	$>17.17$	...	35.2	0.16	1.7
MWC 480	$1.12 \times 10^{-3}$	4.07	...	32.4	...	4.0
TW Hya	$7 \times 10^{-4}$	8	$<0.6$	0.25	0.3	5.6
DM Tau	$2.3 \times 10^{-4}$	5.8	0.44	0.16	0.25	3.4

Note. — Observations presented in the first half of the table are from this survey and those in the second half of the table come from the literature (with CO abundances calculated from  $^{13}\text{CO}$  and  $\text{C}^{18}\text{O}$  column densities, when available). Values for LkCa 15, GM Aur, HD 163296, MWC 480 were obtained at OVRO by Qi (2001). Observations of TW Hya were taken at the JCMT 15m telescope (Kastner et al., 1997). The DM Tau ratios presented in the second half of the table are from Dutrey et al. (1997) obtained with the IRAM 30m telescope.

increases exponentially with the stellar temperature ( $F(T) = \frac{2h\nu^3}{c^2} \exp(-\frac{h\nu}{kT})$ ). Thus, the stellar luminosity should have a large impact on both the temperature of and the stellar UV field at the disk surface.

The CN/CO, HCN/CO and  $\text{HCO}^+/\text{CO}$  abundances as a function of stellar luminosity ( $L_*$ ) for the sources in this sample are shown in Figure 3.3. For comparison, values for other disks for which CN, HCN and  $\text{HCO}^+$  have been observed are also included; these include two T Tauri and two Herbig Ae disks from Qi (2001), LkCa 15, GM Aur, HD 163296 and MWC 480, the nearby T Tauri star TW Hya (Kastner et al., 1997). DM Tau, which is a T Tauri star in our sample, has also been observed with the IRAM 30 m telescope (Dutrey et al., 1997) and the observed abundance ratios are also included here. The abundances are shown relative to CO to remove dependence on the gas mass in the emission region. Although CO is not an effective tracer of the total disk mass, it is a reasonable measure of the mass in disk surface layers to which we are sensitive (see Chapter 2). The observed ratios show no correlation with the stellar luminosity, although they all have similar distributions. This indicates that at the large radii probed by millimeter observations ( $R > 70$  AU), the stellar UV radiation field may not penetrate sufficiently to have a large impact on disk chemistry. This indicates that the interstellar radiation field is very important in photochemical processes in the outer disk, as concluded by Willacy & Langer (2000) in chemical models of disks including the effects of photoprocessing in disk surface layers.

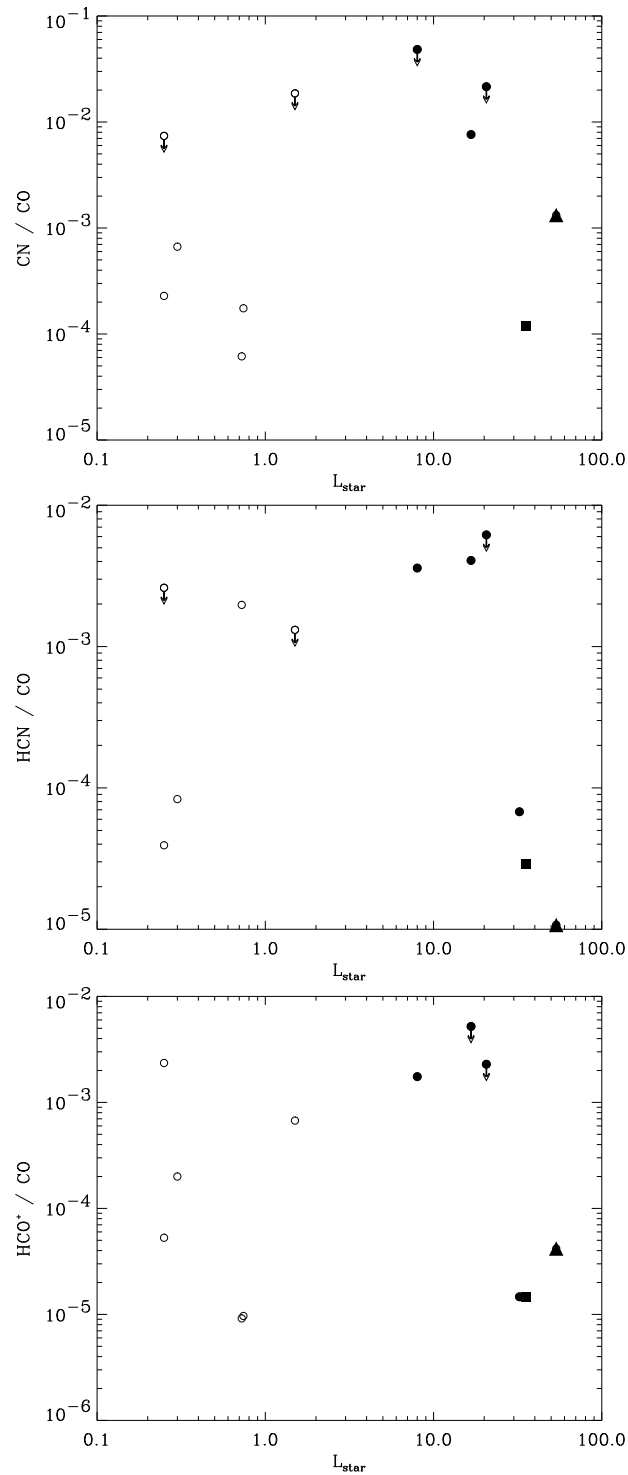


Figure 3.3  $\text{CN}/\text{CO}$ ,  $\text{HCN}/\text{CO}$  and  $\text{HCO}^+/\text{CO}$  abundances shown as a function of stellar luminosity ( $L_*$ ) for all sources observed in this survey (open circles). For comparison, values for other disks are included; LkCa 15, HD 163296, GM Aur, MWC 480 (Qi, 2001) are plotted as filled circles, TW Hya (Kastner et al., 1997) is plotted as a filled triangle and the single dish observation for DM Tau (Dutrey et al., 1997) is plotted as a filled square.

### 3.6.2 Disk flaring and $L_{IR}/L_{bol}$

Dust in the circumstellar disk absorbs stellar radiation and re-radiates it in the IR, such that the luminosity integrated over all wavelengths, or the bolometric luminosity, is a sum of the stellar and reprocessed radiation:

$$L_{bol} = 4\pi d^2 (F_{star} + F_{IR}) \quad (3.43)$$

The fractional IR luminosity  $L_{IR}/L_{bol}$  is thus proportional to the solid angle intercepted by the disk as seen from the star and can be used as a measure of disk flaring (Kenyon & Hartmann, 1995). For YSOs inclined with respect to the observer, the “shadowing” of the star by the disk and foreshortening of the disk must be taken into account. Radiation from the disk decreases as  $\cos i$  (where  $i = 0$  if edge-on). For any disk around a star, the ratio of disk to total flux (disk + star) must be larger than 0.3 (around 0.45) for  $i = 0$ ,  $f_* = 0$  and 0.37 for  $i = 60$ ,  $f_* = 0.29$ . At all inclinations  $L_{tot} > L_{star}$ . While an infinite flat and “passive” disk absorbs and reradiates  $\sim 25\%$  of the stellar flux, “thick” or “flaring” disks with finite scale heights reprocess  $\sim 30\%$ – $40\%$  of the stellar flux. In a large photometric survey of T Tauri stars, Kenyon & Hartmann (1987) find that weak line T Tauri stars, with optically thin disks, have  $L_{IR}/L_{bol} < 0.1$ , while most class II sources possess  $L_{IR}/L_{bol} \approx 0.0$ – $0.3$ . This is a bit higher than that of a random collection of flat reprocessing disks for which  $L_{IR}/L_{bol} = 0.05$  and is suggestive of flared disks ( $L_{IR}/L_{bol} = 0.13$ ). Stars embedded in a spherical envelope of dust, possess much larger fractional IR luminosities  $L_{IR}/L_{bol} > 0.8$  (most  $> 0.9$ ).

Plots of the correlation of  $L_{FIR}/L_{bol}$  with CN, HCN and  $\text{HCO}^+$  abundances relative to CO are shown in Figure 3.4. A weak correlation between the CN/CO and  $\text{HCO}^+$ /CO ratios and the fractional IR luminosity is visible, with the abundances increasing as a function of the IR luminosity. However, there appears to be no correlation between the HCN/CO ratio and  $L_{FIR}/L_{bol}$ . If it is assumed that increased flaring corresponds to increasing the exposure to UV radiation, then this can be explained by the PDR model presented by Fuente et al. (1993) and discussed above in which increased UV fields lead to increased formation of  $\text{C}^+$  and C (and thus  $\text{HCO}^+$ ). This in turn leads to an increase in the production of CH and  $\text{CH}_2$ , and thereby CN and HCN. The increase in HCN production, however, is restricted by an increase in the destruction of HCN through reaction with  $\text{C}^+$  and  $\text{H}^+$ .

### 3.6.3 Dust settling and H/h

Hydrostatic, radiative equilibrium models (Chiang & Goldreich, 1997) indicate that “passive,” flared disks can account for the magnitude of the far-infrared luminosity and the flat shape of SEDs of typical T Tauri stars. In these models, the dust in the disk surface absorbs stellar radiation and re-radiates at IR wavelengths, as discussed above. Approximately half of this reprocessed radiation is directed into space and half radiates into the disk, heating the gas and dust in the surface, and

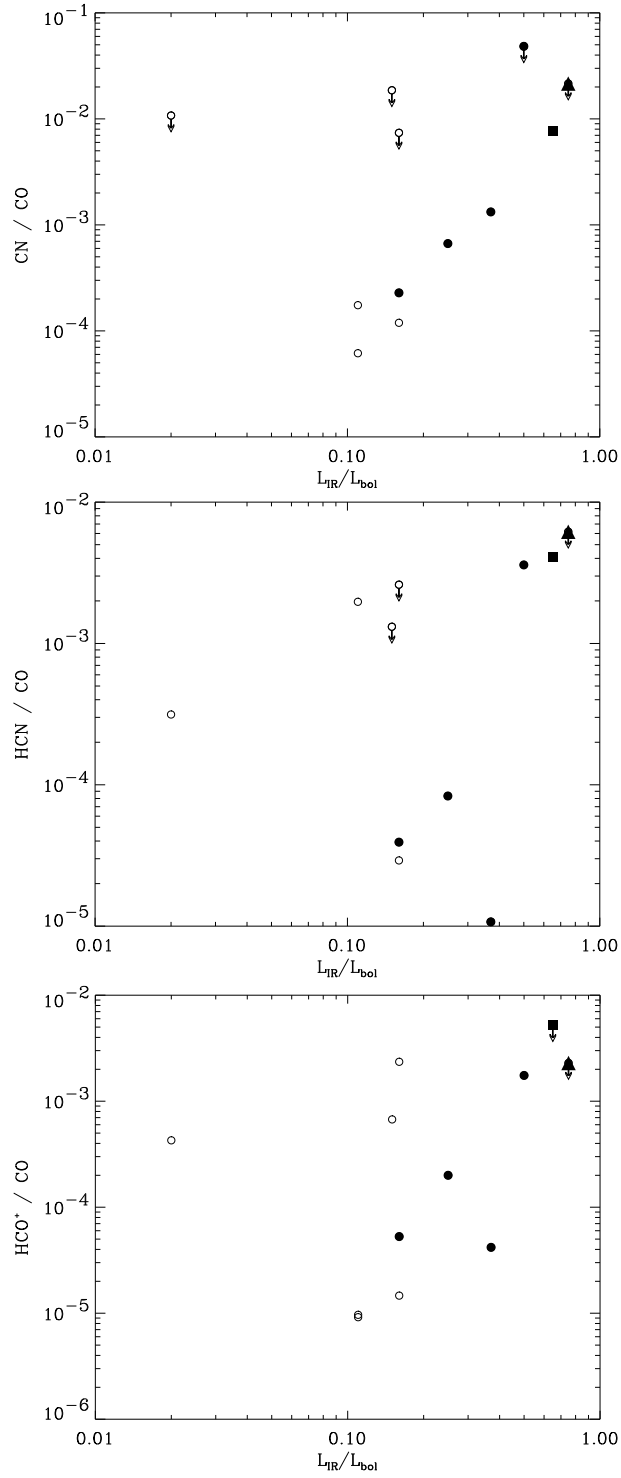


Figure 3.4  $CN/CO$ ,  $HCN/CO$  and  $HCO^+/CO$  abundances shown as a function of the fractional luminosity  $L_{IR}/L_{bol}$ . Points are labeled as in Figure 3.3.

causing the disk to flare. Due to the flared geometry, the surface material is exposed to more stellar radiation and the SED remains flat at longer wavelengths. This can be expressed mathematically as

$$4\pi d^2 \nu F_\nu \approx \alpha L_* \quad (3.44)$$

$$\approx \left[ \left( \frac{d \ln H}{d \ln a} - 1 \right) \frac{H}{a} + \frac{R_*}{a} \right] \frac{L_*}{2}, \quad (3.45)$$

where  $\alpha$  is the angle at which the stellar radiation strikes the surface of the disk,  $H$  is the vertical height of the visible disk photosphere (superheated surface region) above the disk midplane and  $a$  is the radial distance to the disk rotation axis. If we assume that the dust-to-gas ratio is uniform throughout the disk, then the height of the disk photosphere ( $H$ ) and the scale height of the gas ( $h$ ; defined by the condition of hydrostatic equilibrium) can be related through the equation

$$\frac{H}{h} = \left[ 2 \ln \left( \frac{n_0}{n_{ph}} \right) \right]^{1/2}, \quad (3.46)$$

which represents the number of gas scale heights that the visible photosphere sits above the disk midplane. Chiang et al. (2001) systematically explore the dependence of SEDs on grain size distributions, disk geometries and surface densities, and stellar photospheric temperatures and find that this is the most robust parameter in their model.

$H/h$  can be directly related to dust settling. For a disk in which gas and dust are well mixed in interstellar proportions,  $H/h \approx 4-5$  (Chiang & Goldreich, 1997). As dust settles, the height of the photosphere  $H$  decreases faster than the gas scale height and  $H/h$  also decreases. For a dust grain of size  $r$  and mass density  $\rho_p = 2 \text{ g/cm}^3$ , the timescale for sedimentation from height  $z = 4h$  to height  $z = 1h$  is (Creech-Eakman et al., 2002)

$$t_{settle} \approx 0.1 \frac{\Sigma}{\rho_p r \Omega} \quad (3.47)$$

$$\approx 10^5 \left( \frac{0.1 \mu m}{r} \right) \left( \frac{\Sigma_0}{300 \text{ g cm}^{-2}} \right) \left( \frac{2 M_\odot}{M_*} \right)^{1/2} \text{ yr}, \quad (3.48)$$

where  $\Sigma_0$  is the surface density and  $\Omega$  is the local orbital angular frequency of disk material. Thus, for the outer radii of disks ( $\Sigma_0 \sim 1-10 \text{ g cm}^{-2}$  for  $R = 100 \text{ AU}$ ; D'Alessio et al., 2001) surrounding stars in the  $1-3 M_\odot$  range, the timescale for grains to spiral into the midplane of a disk is  $10^5 \text{ yr}$  for  $1 \mu m$  particles and  $\sim 100 \text{ yr}$  for  $1 \text{ cm}$  particles. The stars in the sample studied here have ages of  $\sim 1-10 \text{ Myr}$  and thus we can expect that some growth and sedimentation have occurred.

SEDs for seven of the stars in this sample have been modeled using the Chiang & Goldreich method (Chiang et al., 2001; Chiang & Goldreich, 1997; and private communication), the resulting  $H/h$  values are shown in Table 3.10. There is a large range in  $H/h$  for our sample, with LkCa 15 ( $H/h = 1.0$ ) and CQ Tau ( $H/h = 5.0$ ) representing the two extremes in which the dust has settled

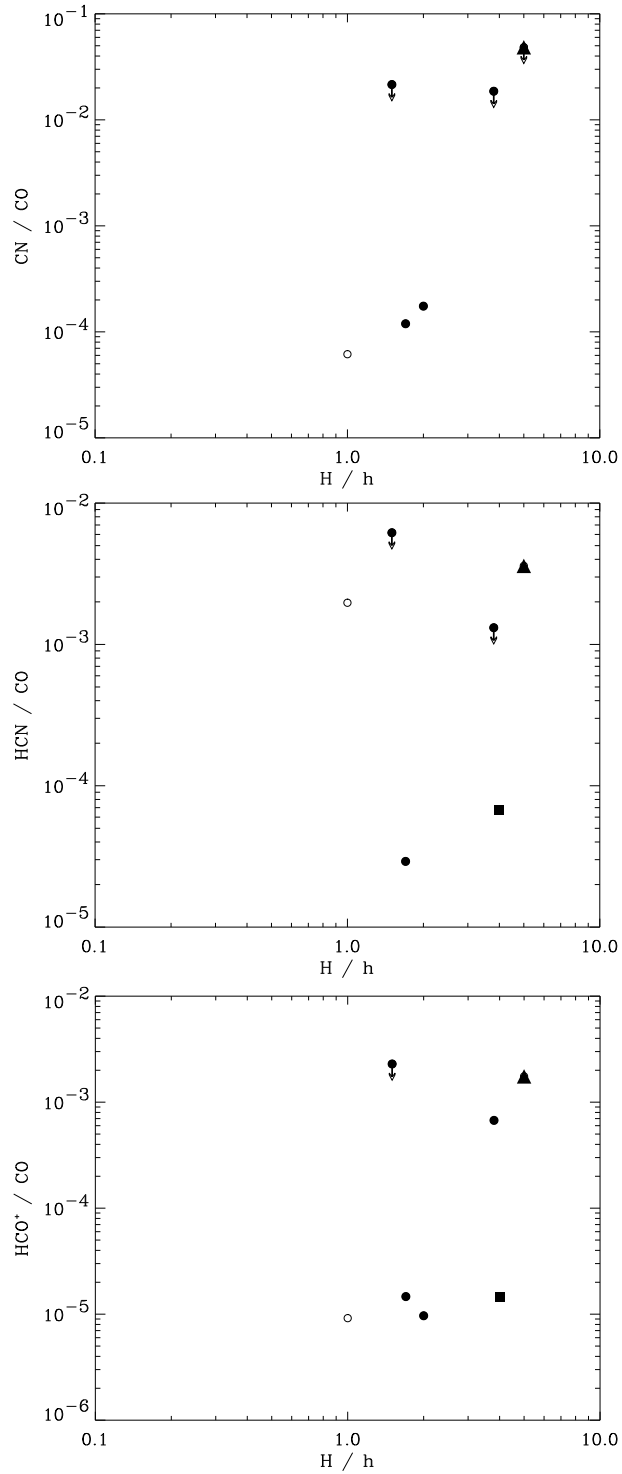


Figure 3.5  $\text{CN}/\text{CO}$ ,  $\text{HCN}/\text{CO}$  and  $\text{HCO}^+/\text{CO}$  abundances shown as a function of the number of scale heights that the visible disk photosphere sits above the disk midplane ( $H/h$ ). Points are labeled as in Figure 3.3.

to the midplane ( $z = 1$ ) and where the gas and dust are uniformly mixed, respectively. As discussed above, the production of CN, HCN and  $\text{HCO}^+$  should be tied to the effective UV field. As dust settles to the disk midplane, the effective UV field is enhanced due to reduced shielding by the dust. To explore this relationship, the fractional abundances of CN, HCN and  $\text{HCO}^+$  (relative to CO) are plotted versus the modeled  $H/h$  dust settling parameter in Figure 3.5. Due to the small sample of sources for which the observed molecules were detected and  $H/h$  values have been calculated, a trend is difficult to establish. However, the distribution of the fractional CN and  $\text{HCO}^+$  abundances with  $H/h$  appear to be quite similar, and quite different than that of HCN. This is similar to what was noted for the fractional IR luminosity  $L_{IR}/L_{bol}$  relations and suggests that both quantities are in fact tracing enhanced effective UV fields in the disk.

### 3.7 Summary

In this study, the  $J = 1-0$  transitions of CO, CN, HCN,  $\text{HCO}^+$  and HNC were observed toward protoplanetary disks surrounding several T Tauri and Herbig Ae stars. The CO and continuum measurements were used to constrain the inclination and radial extent of the disks, but because of the low spatial resolution of the observations ( $4-5''$ ), there are large errors associated with these estimates. It can be stated firmly, however, that the emission from the gas extends to larger radii than that of the dust, as the dust emission was consistently found to be unresolved for all disks in contrast to the CO 1-0 emission. This is likely due to a more rapid fall-off in dust emissivity, and not an absence of dust, at large radii (Sargent & Beckwith, 1987, Qi et al., 2003). The abundances of CO in these disks were found to be consistent with previous observations. The CO and continuum observations were used to calculate the disk gas and dust masses, respectively. Although the gas masses were reasonably consistent with previous observations, the dust masses are consistently too small. This could be due to an observational effect, such as beam dilution, or to variations in the dust opacity, which will have a large effect at the long wavelengths ( $\kappa \propto \nu^\beta$ ; we assumed  $\beta \approx 1$ ). Calculations of the electron fraction for these disks indicated that inclusion of X-ray ionization rates which account for ionization by secondary electrons increases the fractional ionization by  $10^{2-3}$ . Upper limits calculated from the observed  $\text{HCO}^+$  emission do not put significant constraints on the ionization fraction, indicating the importance of other ions, such as  $\text{H}_3^+$  and  $\text{N}_2\text{H}^+$  in disk surfaces.

The effects of UV fields were measured in the disks from observations of CN, HCN and  $\text{HCO}^+$ . Although CN and HCN are produced in a similar manner, through reactions of N with neutral and ionic hydrocarbons, CN is destroyed through neutral-neutral reactions, while HCN is destroyed by ion-molecule chemistry and UV photolysis. An increase in the effective UV field results in increased photoionization, and photodissociation, which in turn leads to increased production of  $\text{HCO}^+$ , CN and HCN. The increase in HCN production, however, is moderated by a coincident increase in

HCN destruction, while the destruction rate of CN remains constant (or decreases). Observations of the CN/HCN ratio should therefore trace the strength of the effective UV field at disk surfaces, with increased CN/HCN corresponding to stronger UV fields. This has been found to be true in molecular clouds and photodissociation regions. In the work presented here, CN, HCN, HNC and HCO<sup>+</sup> were observed toward several circumstellar disks. CN and HCO<sup>+</sup> were found to be (at least weakly) correlated with tracers of the effective UV field; abundances of both molecules increased with increases in the fractional IR luminosity and the dust settling parameter  $H/h$ . HCN, on the other hand, did not appear to be correlated with these or other disk parameters, likely due to the complexity of the reaction network for this molecule. Surprisingly, no molecular abundances appeared to be correlated with stellar parameters, such as  $L_{star}$ . This may indicate that in the outer regions of disks ( $R > 70$  AU) probed by these observations the interstellar radiation field has a much larger effect on the chemistry than the stellar UV field. HNC is produced and destroyed via ion-molecule reactions and thus is expected to be a very good probe of ion-molecule chemistry in disk surfaces. Unfortunately, HNC was only detected toward one source in our sample and a statistical analysis could not be performed, but observations of HNC with more sensitive instruments may prove to be very valuable to improving the understanding of nitrogen chemistry in disks.

The Owens Valley Radio Observatory is supported by the National Science Foundation, AST 9981546. J.E.K. was sponsored by the NASA Graduate Student Researchers Program, NGT5-50231.

### 3.8 Appendix: Integrated intensity maps and spectra for the observed molecules.

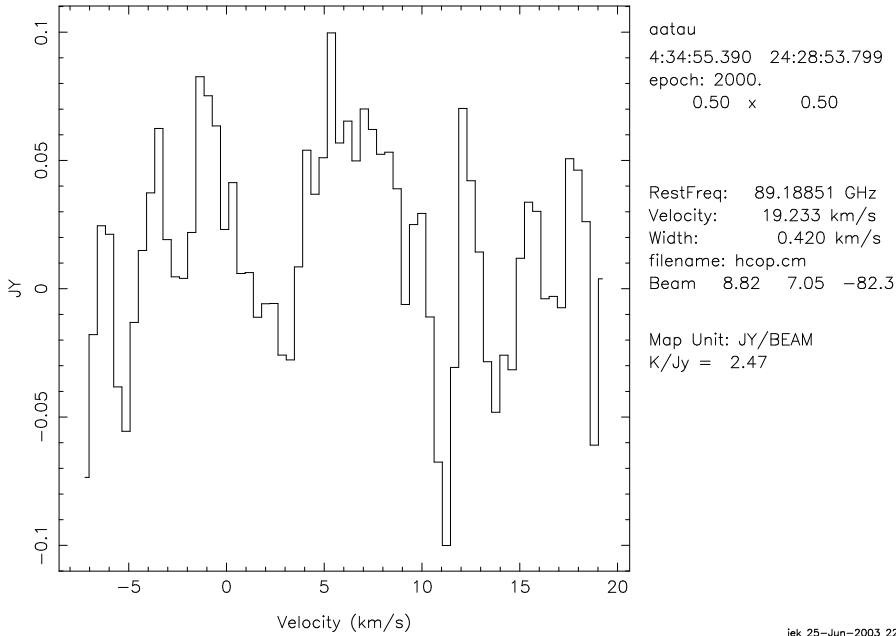
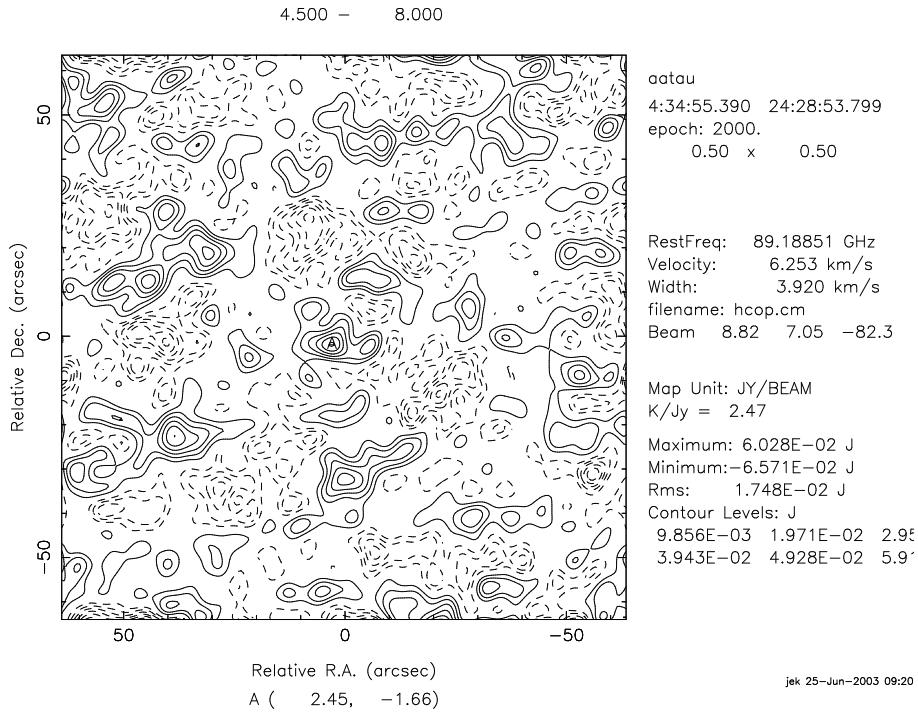


Figure 3.6  $\text{HCO}^+$  1-0 observations toward AA Tau. Although the spectrum is a bit noisy, the moment 0 map shows strong  $\text{HCO}^+$  1-0 emission peaking at the stellar position.

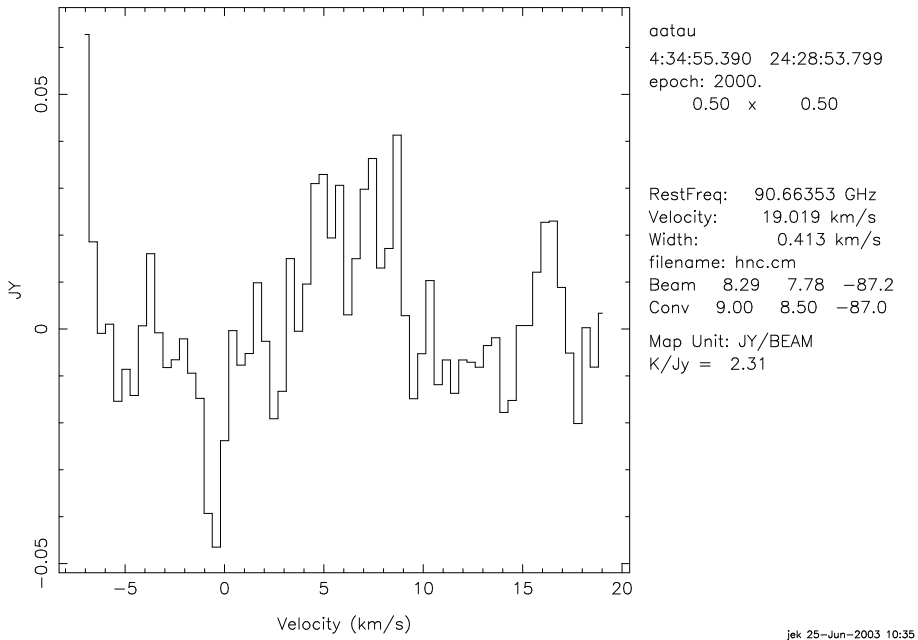
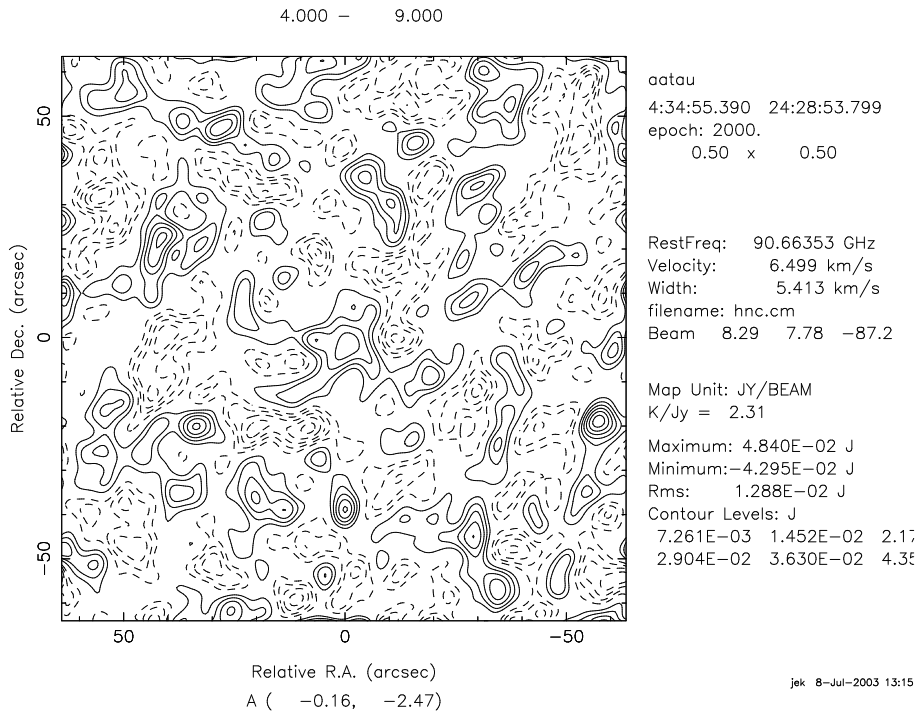


Figure 3.7 HNC 1-0 observations toward AA Tau. HNC emission is strong in the map, although diffuse and clearly visible in the spectrum which is quite similar to that of  $\text{HCO}^+$  and CO 1-0.

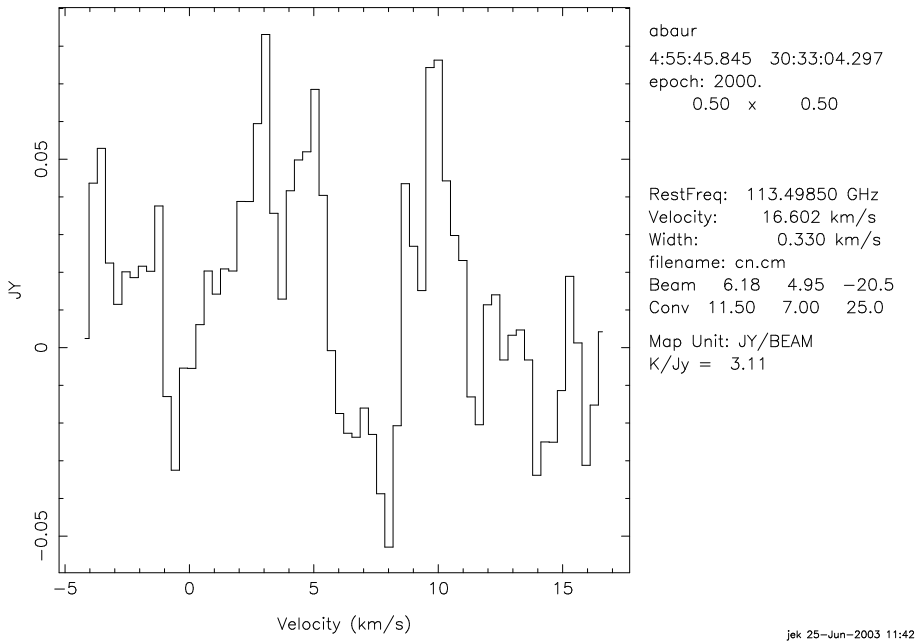
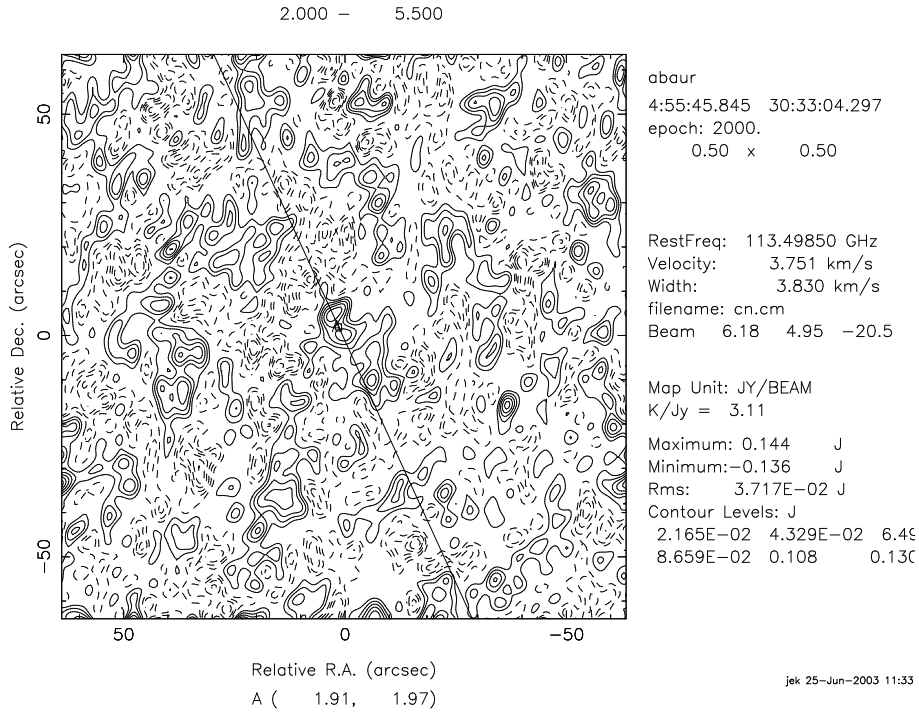


Figure 3.8 CN observations toward AB Aur. CN is strongly detected with a double peak in the map and spectrum.

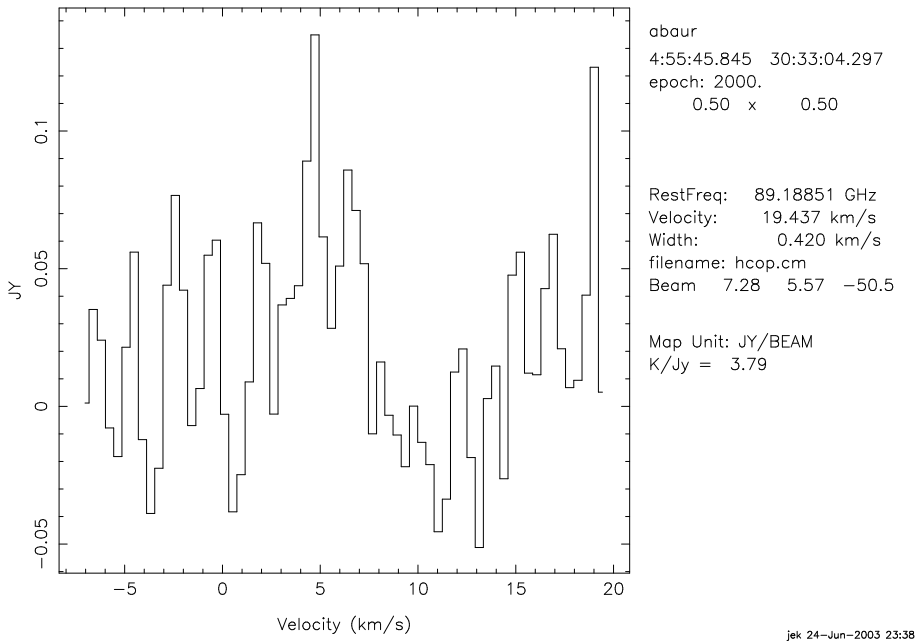
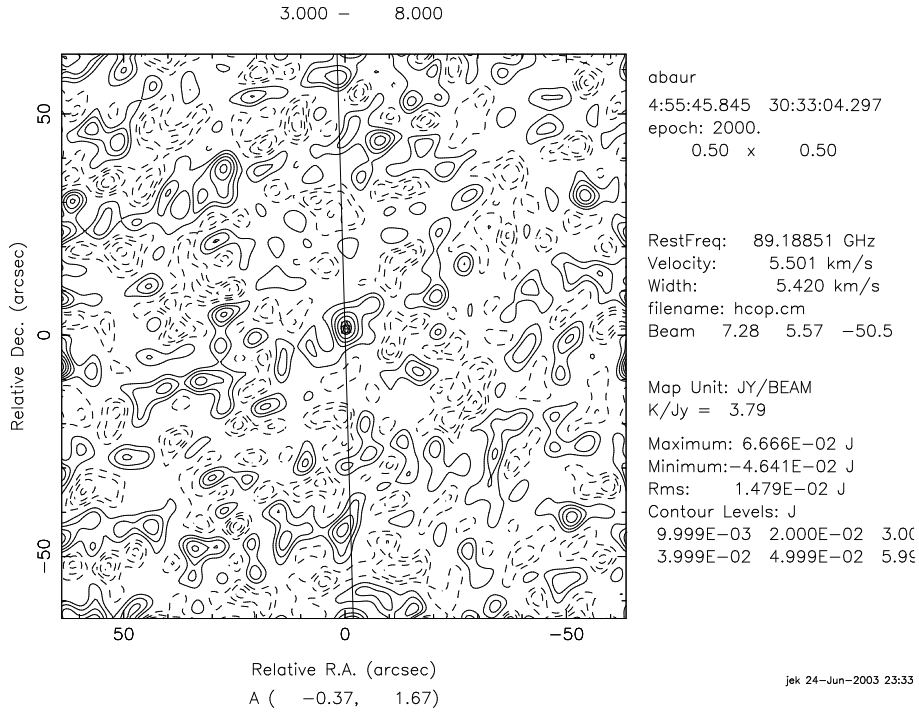


Figure 3.9 HCO<sup>+</sup> observations toward AB Aur.

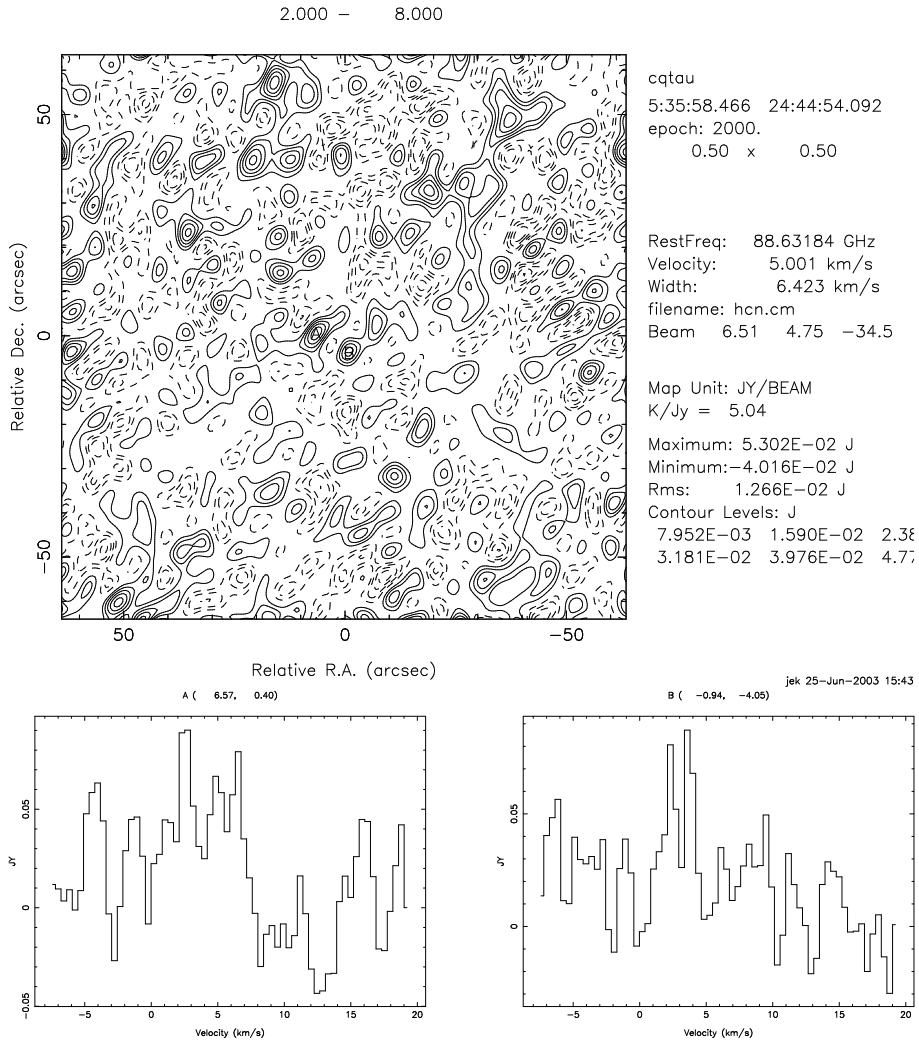


Figure 3.10 HCN observations toward CQ Tau.

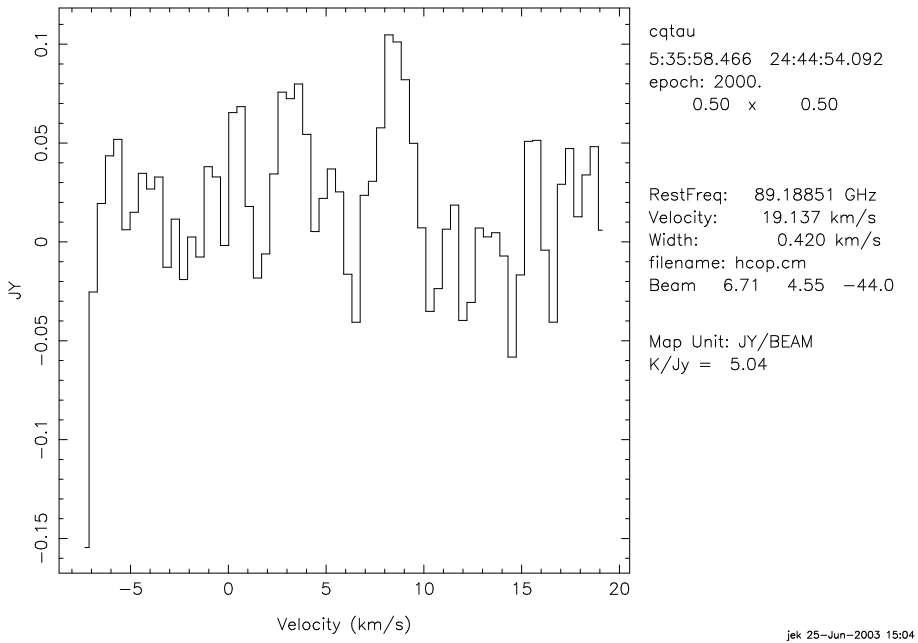
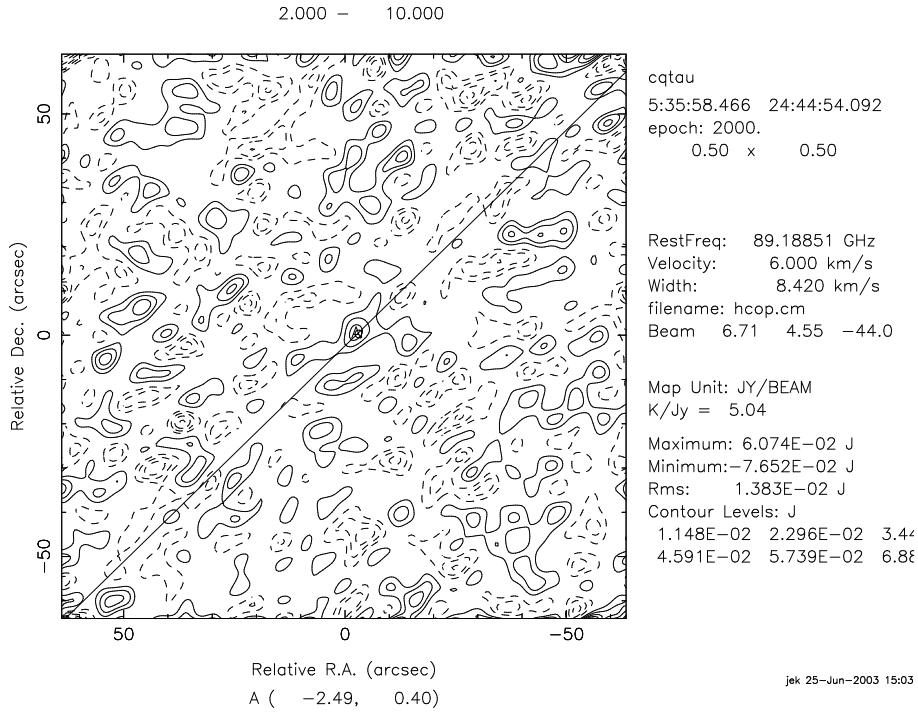


Figure 3.11 HCO<sup>+</sup> observations toward CQ Tau.

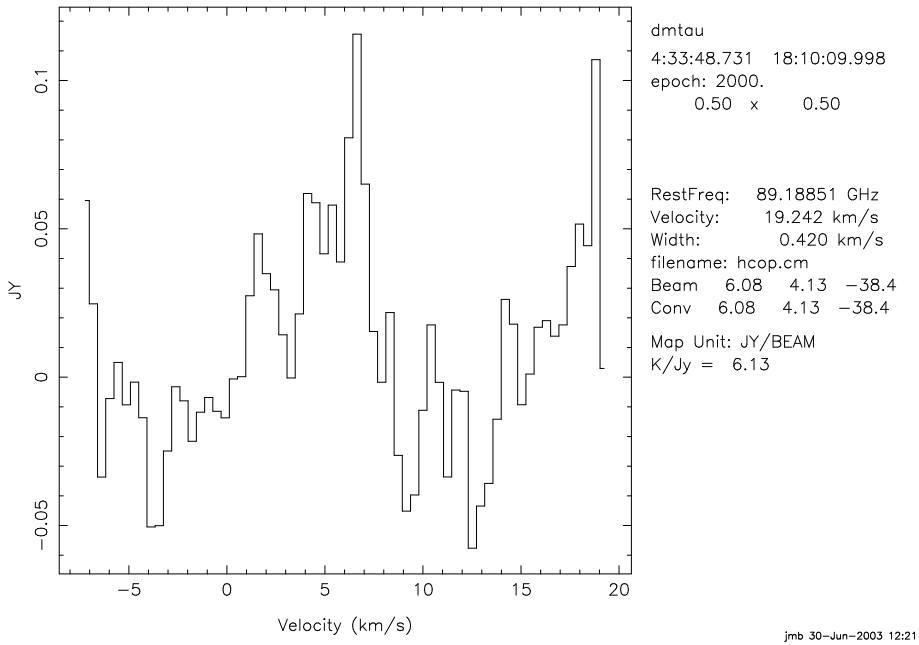
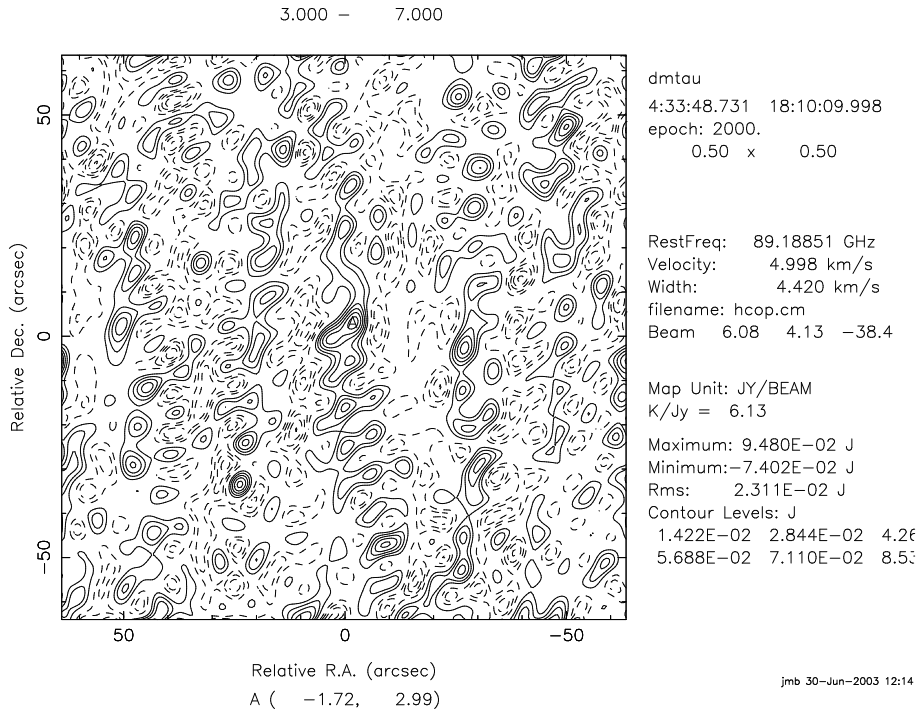


Figure 3.12 HCO<sup>+</sup> observations toward DM Tau.

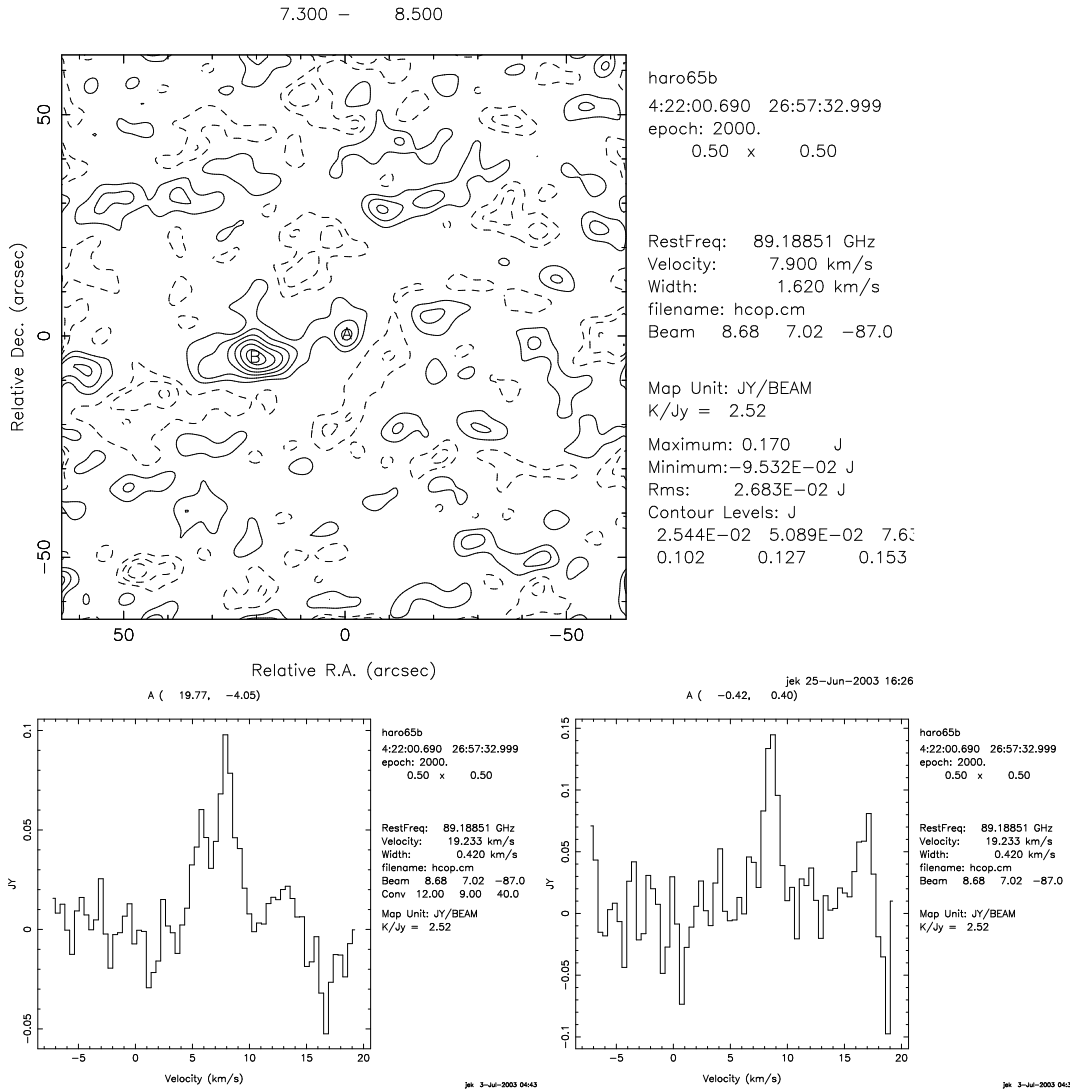


Figure 3.13 HCO<sup>+</sup> observations toward Haro 6-5B (right) and accompanying FS Tau (left).

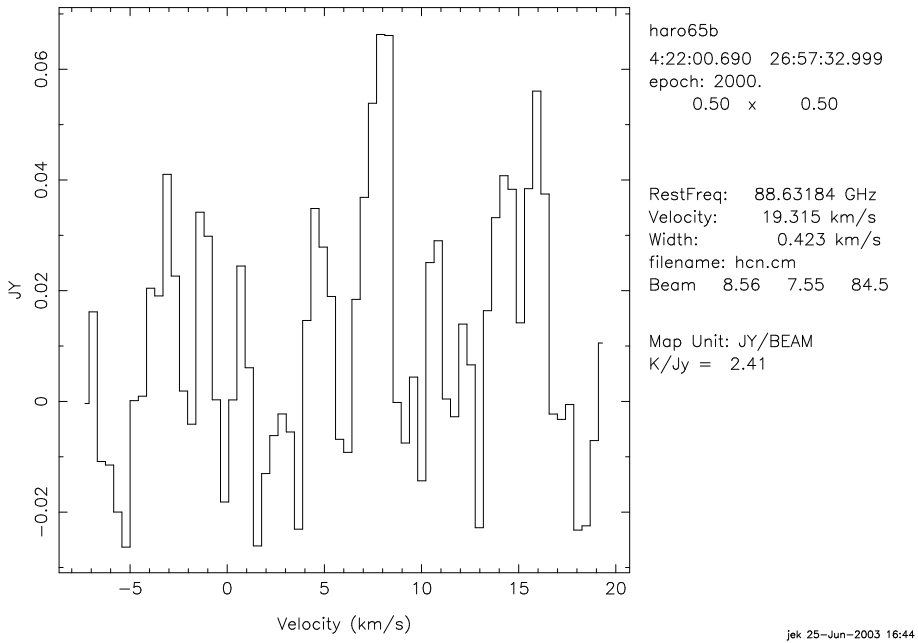
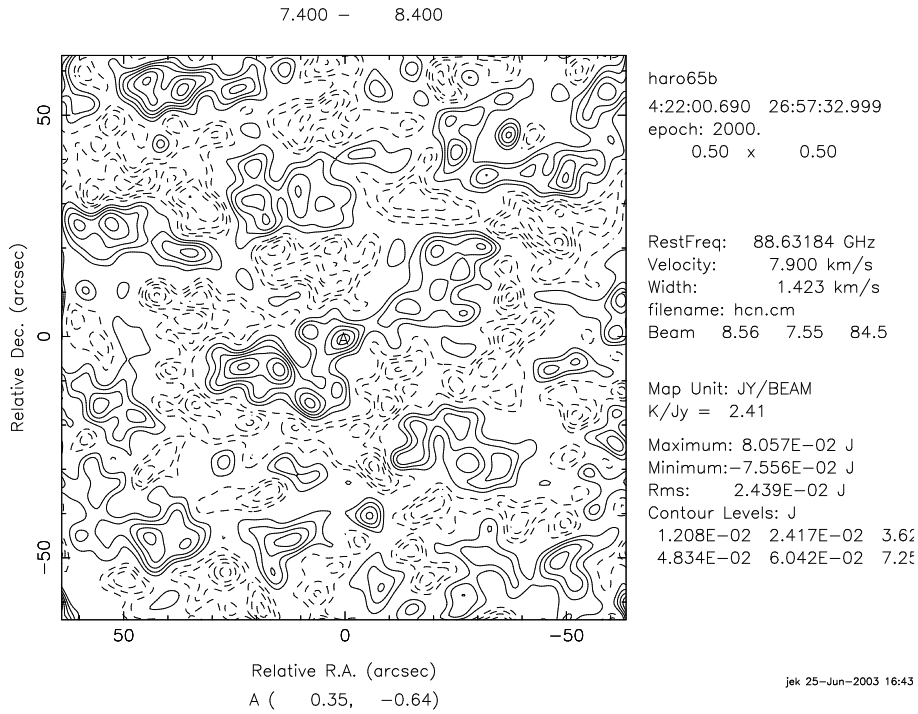


Figure 3.14 HCN observations toward Haro 6-5B.

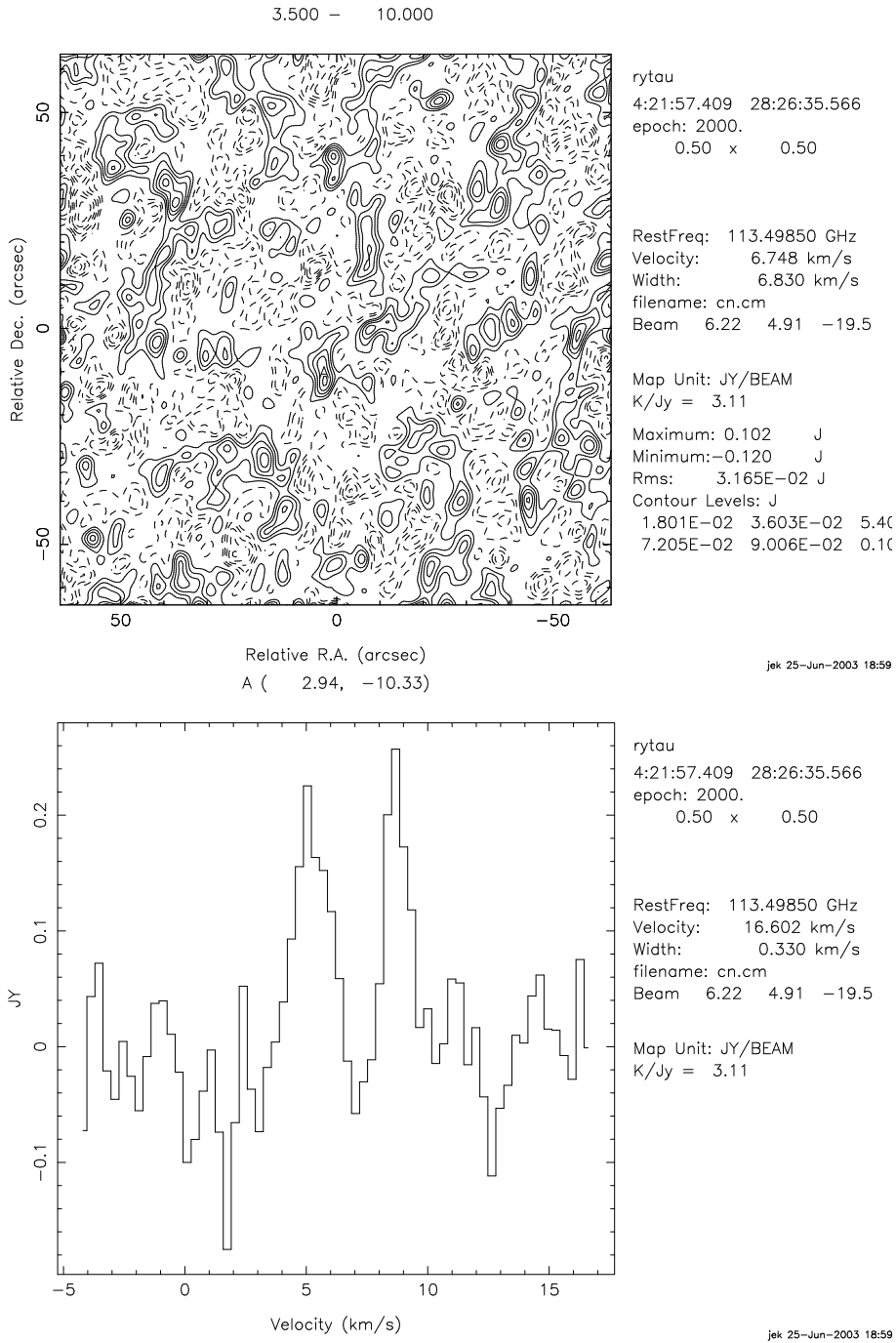


Figure 3.15 CN observations toward RY Tau.

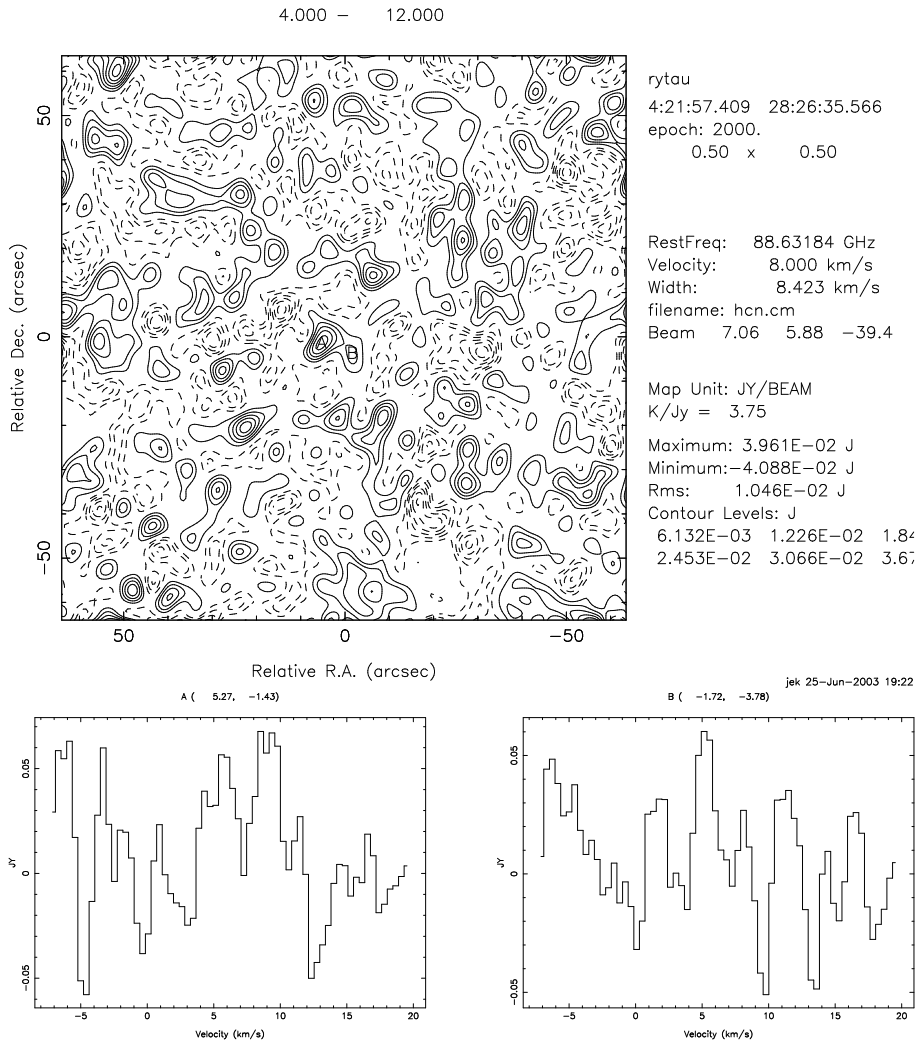


Figure 3.16 HCN observations toward RY Tau. The spectra on the left and right were obtained at points A and B, respectively.

# Bibliography

- Aikawa, Y. & Herbst, E. 1999, *ApJ*, 526, 314
- . 2001, *A&A*, 371, 1107
- Aikawa, Y., van Zadelhoff, G. J., van Dishoeck, E. F., & Herbst, E. 2002, *A&A*, 386, 622
- Bachiller, R., Forveille, T., Huggins, P. J., & Cox, P. 1997, *A&A*, 324, 1123
- Beckwith, S. V. W., Sargent, A. I., Chini, R. S., & Guesten, R. 1990, *AJ*, 99, 924
- Bergin, E., Calvet, N., D'Alessio, P., & Herczeg, G. J. 2003, *ApJ*, 591, L159
- Casanova, S., Montmerle, T., Feigelson, E. D., & Andre, P. 1995, *ApJ*, 439, 752
- Charnley, S. B., Rodgers, S. D., Butner, H. M., & Ehrenfreund, P. 2002, *Earth Moon and Planets*, 90, 349
- Chiang, E. I. & Goldreich, P. 1997, *ApJ*, 490, 368
- Chiang, E. I., Joungh, M. K., Creech-Eakman, M. J., Qi, C., Kessler, J. E., Blake, G. A., & van Dishoeck, E. F. 2001, *ApJ*, 547, 1077
- Cox, P., Omont, A., Huggins, P. J., Bachiller, R., & Forveille, T. 1992, *A&A*, 266, 420
- Creech-Eakman, M. J., Chiang, E. I., Joungh, R. M. K., Blake, G. A., & van Dishoeck, E. F. 2002, *A&A*, 385, 546
- D'Alessio, P., Calvet, N., & Hartmann, L. 2001, *ApJ*, 553, 321
- D'Alessio, P., Calvet, N., Hartmann, L., Lizano, S., & Cantó, J. 1999, *ApJ*, 527, 893
- Damiani, F., Micela, G., Sciortino, S., & Harnden, F. R. 1995, *ApJ*, 446, 331
- Duley, W. W. & Williams, D. A. 1984, *Inorganic Chemistry*
- Dutrey, A., Guilloteau, S., Duvert, G., Prato, L., Simon, M., Schuster, K., & Menard, F. 1996, *A&A*, 309, 493

- Dutrey, A., Guilloteau, S., & Guelin, M. 1997, *A&A*, 317, L55
- Duvert, G., Guilloteau, S., Ménard, F., Simon, M., & Dutrey, A. 2000, *A&A*, 355, 165
- Feigelson, E. D. & Montmerle, T. 1999, *ARA&A*, 37, 363
- Fuente, A., Martin-Pintado, J., Cernicharo, J., & Bachiller, R. 1993, *A&A*, 276, 473
- Glassgold, A. E., Najita, J., & Igea, J. 1997, *ApJ*, 480, 344
- Herbig, G. H. & Goodrich, R. W. 1986, *ApJ*, 309, 294
- Herbst, E., Defrees, D. J., & McLean, A. D. 1987, *ApJ*, 321, 898
- Igea, J. & Glassgold, A. E. 1999, *ApJ*, 518, 848
- Imhoff, C. L. & Appenzeller, I. 1987, in *ASSL Vol. 129: Exploring the Universe with the IUE Satellite*, 295–319
- Jansen, D. J., van Dishoeck, E. F., Black, J. H., Spaans, M., & Sosin, C. 1995, *A&A*, 302, 223
- Johansson, L. E. B., Andersson, C., Ellder, J., Friberg, P., Hjalmarsen, A., Hoglund, B., Irvine, W. M., Olofsson, H., & Rydbeck, G. 1984, *A&A*, 130, 227
- Johnstone, R. M. & Penston, M. V. 1986, *MNRAS*, 219, 927
- Kastner, J. H., Zuckerman, B., Weintraub, D. A., & Forveille, T. 1997, *Science*, 277, 67
- Kenyon, S. J. & Hartmann, L. 1987, *ApJ*, 323, 714
- . 1995, *ApJ*, 101, 117
- Koerner, D. W. & Sargent, A. I. 1995, *AJ*, 109, 2138
- Langer, W. D. & Graedel, T. E. 1989, *ApJS*, 69, 241
- Lay, O. P. 1997, *A&AS*, 122, 547
- Mannings, V. & Sargent, A. I. 1997, *ApJ*, 490, 792
- . 2000, *ApJ*, 529, 391
- Millar, T. J., Bennett, A., Rawlings, J. M. C., Brown, P. D., & Charnley, S. B. 1991, *A&AS*, 87, 585
- Millar, T. J., Farquhar, P. R. A., & Willacy, K. 1997, *A&AS*, 121, 139
- Montmerle, T. 1992, *Memorie della Societa Astronomica Italiana*, 63, 663

- Nakano, T. & Tadamaru, E. 1972, *ApJ*, 173, 87
- Nee, J. B. & Lee, L. C. 1985, *ApJ*, 291, 202
- Neuhaeuser, R., Sterzik, M. F., Schmitt, J. H. M. M., Wichmann, R., & Krautter, J. 1995, *A&A*, 297, 391
- Nuth, J. A. & Glicker, S. 1982, *Journal of Quantitative Spectroscopy and Radiative Transfer*, 28, 223
- Pickett, H. M., Poynter, R. L., Cohen, E. A., Delitsky, M. L., Pearson, J. C., & Muller, H. S. P. 1998, *Journal of Quantitative Spectroscopy and Radiative Transfer*, 60, 883
- Pineau des Forets, G., Roueff, E., & Flower, D. R. 1990, *MNRAS*, 244, 668
- Prasad, S. S. & Huntress, W. T. 1980, *ApJS*, 43, 1
- Qi, C. 2001, PhD thesis, California Institute of Technology
- Qi, C., Kessler, J. E., Koerner, D. W., Sargent, A. I., & Blake, G. A. 2003, *ArXiv Astrophysics e-prints*
- Sargent, A. I. & Beckwith, S. 1987, *ApJ*, 323, 294
- Sault, R. J., Teuben, P. J., & Wright, M. C. H. 1995, in *ASP Conf. Ser. 77: Astronomical Data Analysis Software and Systems IV*, 433–+
- Scoville, N. Z., Carlstrom, J. E., Chandler, C. J., Phillips, J. A., Scott, S. L., Tilanus, R. P. J., & Wang, Z. 1993, *PASP*, 105, 1482
- Scoville, N. Z., Sargent, A. I., Sanders, D. B., Claussen, M. J., Masson, C. R., Lo, K. Y., & Phillips, T. G. 1986, *ApJ*, 303, 416
- Spaans, M. 1996, in *IAU Symp. 178: Molecules in Astrophysics: Probes & Processes*, 431
- Sternberg, A. & Dalgarno, A. 1995, *ApJS*, 99, 565
- Tielens, A. G. G. M. & Hollenbach, D. 1985, *ApJ*, 291, 747
- Turner, B. E., Pirogov, L., & Minh, Y. C. 1997, *ApJ*, 483, 235
- Umebayashi, T. & Nakano, T. 1981, *PASJ*, 33, 617
- van Zadelhoff, G.-J. 2002, PhD thesis, Leiden University, The Netherlands
- van Zadelhoff, G.-J., van Dishoeck, E. F., Thi, W.-F., & Blake, G. A. 2001, *A&A*, 377, 566
- Willacy, K. & Langer, W. D. 2000, *ApJ*, 544, 903
- Zinnecker, H. & Preibisch, T. 1994, *A&A*, 292, 152